Bore Sight Error analysis in seeker antennas: A fully functional GUI interfaced Ray Tracing Solution

by

Daniel David Barnard

Thesis presented in partial fulfilment of the requirements for the degree of Master of Science in Engineering at Stellenbosch University

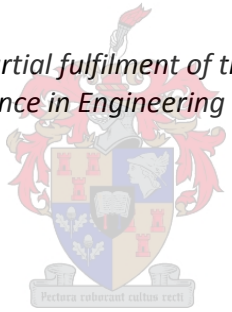

Supervisor: Prof K.D. Palmer
Department of Electrical and Electronic Engineering

March 2013

Declaration

By submitting this thesis electronically, I declare that the entirety of the work contained therein is my own, original work, that I am the sole author thereof (save to the extent explicitly otherwise stated), that reproduction and publication thereof by Stellenbosch University will not infringe any third party rights and that I have not previously in its entirety or in part submitted it for obtaining any qualification.

March 2013

Abstract

Airborne seeker antennas are usually enclosed within a dielectric radome for protection against their harsh operational environment. However the presence of a radome can introduce serious degrading effects on the radiation and electrical performance of the enclosed antenna. The degradation effect studied in this report is that of Bore Sight Error (BSE). BSE is a squint in the pointing accuracy of the antenna due to the enclosing radome. A ray-tracing approach is presented that is able to analyse the BSE of seeker radomes in general and is especially suited to electrically large radomes where other computational electromagnetic techniques become overly computationally intensive.

The ray-tracing algorithm is wrapped in a GUI which, given the radome, antenna, polarisation and incidence plane parameters will compute the BSE for any set of requested scan angles. Close agreement was obtained with measured BSE performance available in literature. Due to easy setup and fast computation time it is demonstrated that the GUI can be efficiently used for iterative radome design and optimisation.

Opsomming

Luggedrae soekantennes is normaalweg omhul binne ‘n dielektriese antennekoepel vir beskerming teen ‘n strawwe omgewing. Die teenwoordigheid van ‘n antennakoepel kan egter ernstige nadelige effekte op die straling en elektriese werkverrigting van die omhulde antenne hê. Die nadelige effek wat in hierdie verslag ondersoek word, is dié van die “Bore Sight Error (BSE).” BSE is ‘n afwyking in die akkuraatheid van die antenna se rigtingwysing as gevolg van die antennakoepel. Straal-natrekking wat die BSE van soek-antennekoepels in die algemeen kan analiseer word beskryf. Hierdie tegniek is veral gepas vir elektries groot antennekoepels waar die berekenige vir EM tegnieke te intensief raak.

Die straalnatrekkingsalgoritme word omvat in ‘n grafiese gebruikerskoppelvlak. Gegee die parameters van die antennekoepel, antenne, polarisasie en invallende vlak, sal die BSE vir enige stel skandeerhoeke bereken word. Goeie ooreenstemming was verkry, vergeleke met gemete BSE vanuit die literatuur. Die eenvoudige opstel van die koppelvlak en vinnige berekeningstyd wys daarop dat die koppelvlak doeltreffend gebruik kan word vir iteratiewe antennekoepel ontwerp en optimering.

Acknowledgements

- My Lord and saviour who provided me with the knowledge, perseverance and strength to finish this project
- My family and friends, especially my wife Lené, for their prayers and support
- Prof K.D. Palmer
- My colleagues at Antenna Magus

Table of Contents

List of Figures

List of Tables

Abbreviations

- BOR – Body of revolution
- BSE – Bore Sight Error
- BSES – Bore Sight Error Slope
- EM – Electromagnetic
- FFT – Fast Fourier Transform
- IP – Insertion phase
- LHC – Left Hand Circular
- RHC – Right Hand Circular
- SEP – Surface Equivalence Principle
- TE – Transverse Electric
- TM – Transverse Magnetic
- λ_m – Wavelength in the dielectric medium
- λ – Free-Space Wavelength

1 Introduction

The word radome is a portmanteau of radar and dome. It is a structural, weatherproof enclosure that protects a microwave or radar antenna. Ironically, although the word dome is present, many radomes are not dome shaped and do not necessarily cover radar antennas.

The primary function of a radome is to protect the antenna system from the environmental conditions encountered in various applications such as shipboard, ground-based, or airborne. The shape of the radome is obviously dependent on the application and on the type of antenna system which it encloses. A mechanically scanned antenna for instance must be enclosed by a radome with a sufficient internal volume for scanning to take place without the antenna interfering with the radome. In some applications the radome is also used to protect nearby personnel from being accidently struck by a quickly rotating antenna.

Of equal importance as its primary environmental protection role is that a radome must be designed to have an almost insignificant effect on the electrical performance of the enclosed antenna. For this reason radomes are generally designed using low-loss dielectric shells, with a radome wall thickness comparable to half the wavelength of operation.

The radome application investigated in this thesis is that of a seeker missile as might be deployed in a long range air-to-air role. As stated above, the application determines the radomes design parameters (shape, radome wall thickness, internally enclosed volume etc.). The application at hand requires aerodynamic radomes which are usually electrically large. The electromagnetic (EM) solution of such problems requires large amounts of computational resources and long simulation times, making the design of electrically large radomes a long and tedious process.

Problem statement:

The purpose of this work is firstly, to investigate and develop an efficient ray tracing code for the modelling of electrically large radomes and secondly, to develop a functional GUI which interfaces with the ray tracing code so as to expand its usability.

Besides this introduction this thesis is structured as follows:

- In Chapter 2 the reader is presented with a discussion on radome design considerations and various well-known computational EM techniques potentially applicable to the solution of electrically large radome problems.
- In Chapter 3 a detailed investigation of one of these techniques, viz. modelling the radome wall as a flat slab, will be discussed.
- In Chapter 4 the technique investigated in Chapter 3 is incorporated into the main algorithm used to investigate the radomes electrical performance when applied to a practical design problem. The user interface designed is described at the end of Chapter 4.
- In Chapter 5 the solution method of Chapter 4 is applied to a further example to prove the validity of the method. The usefulness of the user interface is also highlighted in this Chapter.
- The thesis is concluded in Chapter 6 with a summary and recommendations for further research.

2 Literature Study

Before the analysis and design of the simulation technique is discussed, a review of some of the more important aspects of radome design and analysis is needed. Two main themes are discussed in this introductory chapter: the first is that of the radome design considerations and the second, is the EM techniques used to solve electrically large radomes. The chapter also introduces the reader to the terminology and key concepts which will be investigated in later chapters.

2.1 Design Considerations

As stated in the introduction, radome design is a multifaceted discipline between mechanical, electrical and environmental specifications. These conflicting disciplines will, in many cases, result in a delicate balance being struck in order to achieve an acceptable compromise. The following sections provide a broad description of the different design considerations effecting radome design.

2.1.1 Mechanical Design Considerations

The mechanical design specifications of a radome vary drastically from one application to another. For instance, a radome required for a supersonic airborne application will have much tighter design specifications on weight when compared to a ground based application radome. The shape, strength, material used, to name a few, all play a substantial role in the mechanical design. A few fairly well documented mechanical design constraints are discussed next.

2.1.1.1 Radome Shape

The investigation here is limited to airborne missile type radomes and only the most well-known shapes applicable to this field are discussed. These shapes, together with others are presented in [1] and in the unpublished paper [2].

Figure 2.1 shows the parameter definitions used in the different nose shape defining equations. The equations define a 2D profile of the radome, which, when rotated around the radome centreline (C/L) , forms a full body of revolution (BOR). Parameters defined are the overall radome length (L), base radius (R) and the radome radius (y) at any distance (x) from the radome tip. The equations represent a "perfect" radome shape. Practical radomes may have a blunted or truncated tip due to manufacturing or aerodynamic reasons.

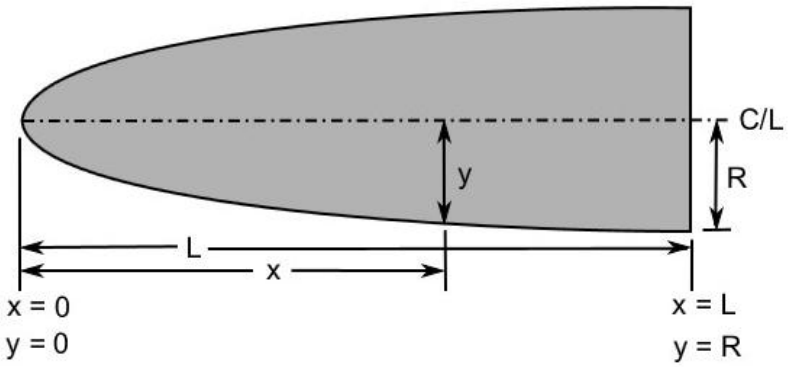

Figure 2.1: Dimensions used for the radome shape equations (adapted from [2])

The radome profiles investigated are the conical, power series, tangent ogive and the Haack series. The Haack and power series look similar to the shape in Figure 2.1 whilst the tangent ogive and conical shapes are presented in Figure 2.2 below.

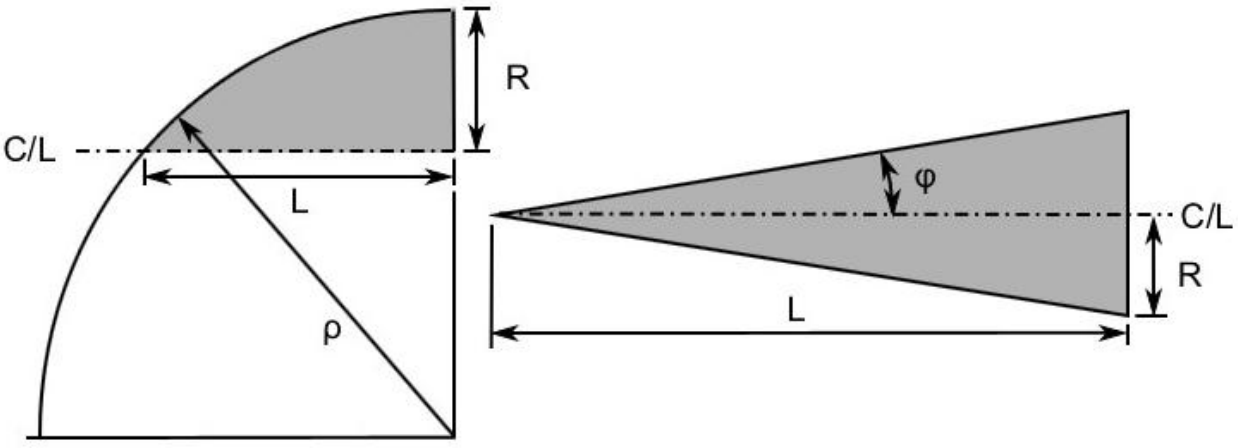

Figure 2.2: Tangent Ogive (left) and conical (right) radome profile shapes (adapted from [2])

The *conical* profile is the most basic and is often used due to its ease of manufacturing. It is often chosen for its favourable drag characteristics at low speeds, however, at higher speeds these become poor. This profile can be defined using the cone angle $(\emptyset)$ in Eq. 2.1 and Eq. 2.2 or by using the overall radome length and base radius in Eq. 2.3. [2]

$$\emptyset = arctan(\frac{R}{L}) \tag{2.1}$$

$$y = xtan\emptyset \tag{2.2}$$

$$y = \frac{xR}{L} \tag{2.3}$$

The *power series* profile, shown in Figure 2.1, includes the shape commonly known to modellers as the "parabolic" nose cone. This series is characterised by its (usually) blunt tip and by the fact that the base is not tangential to the missile body tube forming a discontinuity which looks distinctly non-aerodynamic. Modifications to this discontinuity are sometimes made to produce a smooth nose cone to body transition. [2]

This shape is generated by rotating a parabola about its centreline and is defined by Eq. 2.4

$$y = \left(\frac{xR}{L}\right)^n \qquad For\ 0 \leq n \leq 1 \tag{2.4}$$

The factor “n” controls the bluntness of the nose cone profile. As this factor decreases, the nose becomes increasingly blunt whilst above 0.7, the shape is relatively sharp. Other interesting values of n produce the following profiles: cone (n=1), ¾ power series (n=0.75), parabola (n=0.5) and a cylinder (n=0). The power series family therefore contains a number of nose cone shapes by varying one factor.

Together with the simple conical shape, the *tangent ogive* is the most familiar in hobby rocketry. This is predominantly due to the ease of construction. The profile, shown in Figure 2.2, is formed by a segment of a circle such that the rocket body is tangential to the curve of the nose cone at its base; the base being on the radius of the circle. The Ogive Radius (ρ) is the radius of the arc which forms the profile. The defining equations for the tangent ogive profile are given below. Interestingly, when the length of the nose cone and the ogive radius are equal, a hemisphere is formed. [2]

$$\rho = \frac{R^2 + L^2}{2R} \qquad L \leq \rho \tag{2.5}$$

$$y = \sqrt{\rho^2 - (x - L)^2} + (R - \rho) \tag{2.6}$$

Unlike any of the three shapes discussed above, the *Haack series* is mathematically derived to minimise drag, and is therefore not constructed from geometrical figures. The series is a continuous set of shapes described by θ (Eq. 2.7) and by the value of the c-factor(C) in Eq. 2.8. Two values of the c-factor have particular significance, namely C = 0 noted as “LD” and C= 1/3 known as “LV”. “LD” signifies a design of minimum drag for a given length and diameter and is known as the LD-Haack or Von Karman Ogive. “LV” signifies minimum drag for a given length and volume and is known as the LV-Haack profile. The Haack profile also has a slight discontinuity at the missile body, however, it is so slight that it is assumed to be negligible. [2]

$$\theta = arccos\left(1 - \frac{2x}{L}\right) \tag{2.7}$$

$$y = \frac{R\sqrt{\theta - \frac{sin(2\theta)}{2} + Csin^3\theta}}{\sqrt{\pi}} \tag{2.8}$$

2.1.1.2 Aerodynamic Considerations

Aerodynamic considerations play a major role in radome design, especially in the profile shape and the material used. The radome shape sets the aerodynamic drag whereas the materials determine the response to aerodynamic heating, dynamic pressure and rain erosion [3].

The two parameters, drag and structure, are not independent of each other, and moreover, the electrical performance is very much a function of these two. Fortunately, the shapes that provide the best drag performance are those that lend themselves to meeting the structural performance criteria. The most desirable shapes from a drag point of view are unfortunately not necessarily the best from an electrical performance point of view. The decision to optimise for drag performance determines the outer shape of the radome in virtually all airborne radome applications [3].

An excellent overview of radome shapes and the aerodynamic characteristics and considerations of missile design are presented in [1]. This field is extremely complex, so only some of the important aspects of aerodynamic design are highlighted next.

Below speeds of Mach 0.8, the *nose pressure drag* is virtually zero for most radome shapes. At these speeds, the major contributor to the drag is due to (skin) *frictional drag*. Frictional drag is largely dependent on the *wetted area*, the smoothness thereof and the presence of any discontinuities in this area. The wetted area of a nose cone is the total surface area that is exposed to airflow, excluding the base area of nose cone. Equations for determining the wetted area of a radome shape are presented in [2]. For subsonic model flight, a short, blunt, smooth elliptical shape is usually aerodynamically best.

As stated previously, pressure or form drag in the subsonic region is generally small and may be neglected in preliminary design studies. However, in the transonic and supersonic region pressure drag constitutes a great percentage of the total drag of the missile and must therefore be carefully considered for missile performance design [1]. The factors influencing the pressure drag are the general shape of the nose cone, its *fineness ratio* and its *bluffness ratio* [2].

The fineness ratio, also known as the ‘Aspect ratio’ or ‘Caliber’ of a nose cone, is the ratio of the nose cone length to the base diameter. This ratio at supersonic speeds has a very significant effect on the nose cone wave drag, especially for low ratios. Very little additional gain for a fineness ratio greater than 5 has been documented. One thing to keep in mind is that as the fineness ratio increases, the wetted area and thus skin friction drag component will also increase. Therefore the

minimum drag fineness ratio will be a trade-off between the decreasing wave drag and increasing friction drag [2].

The sharp tip of the nose cone is often blunted to some degree as a practical matter for ease of manufacturing, resistance to handling and flight damage, and safety. This blunting is most often specified as a hemispherical 'tip diameter' of the nose cone. The term '*Bluffness Ratio*' is often used to describe a blunted tip and is set equal to the tip diameter divided by the base diameter. There is little to no drag increase for a slight blunting of the tip. It has been stated by [1] and [2] that there is in fact a decrease in frictional drag for bluffness ratios of up to 0.2 for an overall constant nose cone length. This ratio can, however, have an effect on the pressure drag: an increase in bluffness ratio causes a decrease in fineness ratio.

Figure 2.3 is the most comprehensive and useful compilation of data for comparing the drag characteristics of different nose cone shapes at different Mach speeds. What is evident is that the shapes that have a more superior ranking are slightly rounded at the tip and are not conical as may be imagined.

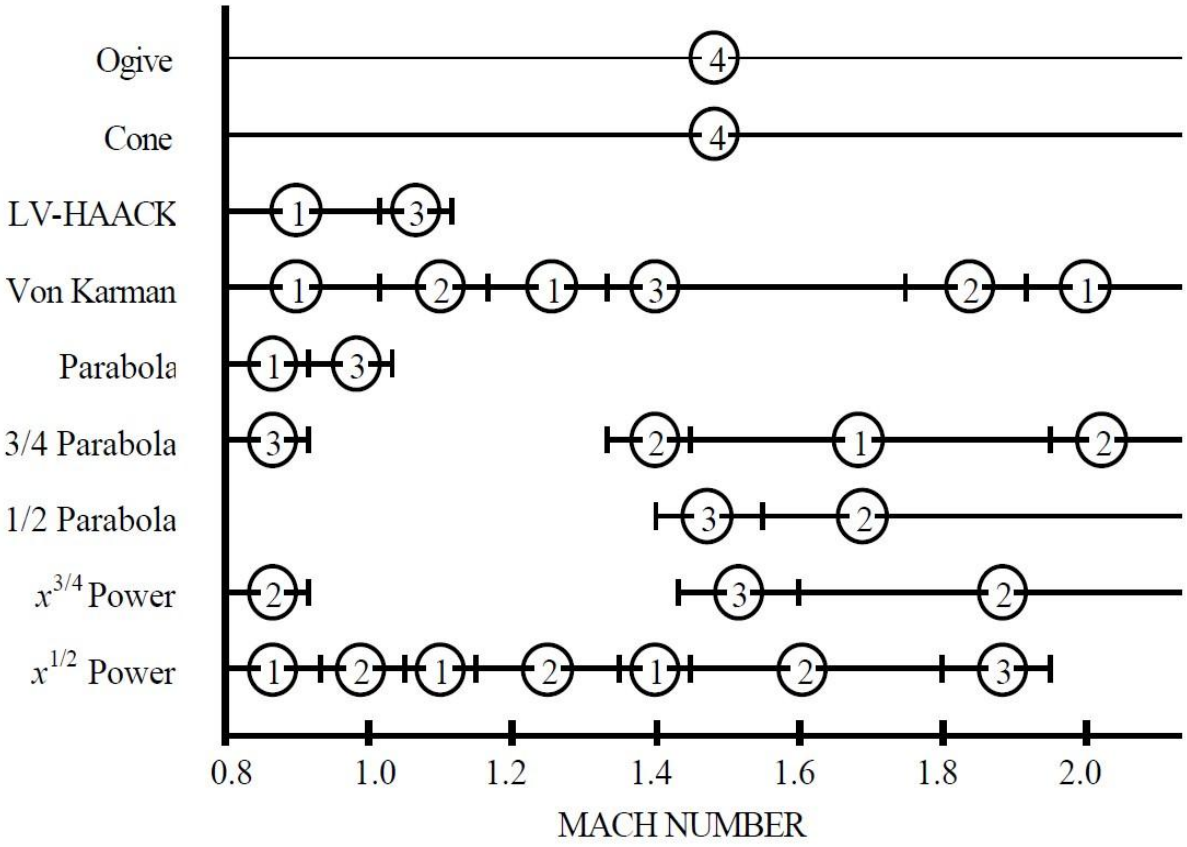

Figure 2.3: Drag characteristics for various nose cone shapes in the transonic-to-low Mach regions. Rankings are: superior (1), good (2), fair (3), inferior (4). [2]

A further mechanical design consideration is the mechanical stresses produced on the radome by aerodynamic loading due to airflow, acceleration forces, and sudden thermal expansion due to aerodynamic heating. In high speed radomes, thermal shock often causes the highest mechanical stresses. These stresses are greatest in the nose region, which will often contain a metallic tip that must be integrated into the design [4].

The attachment point of the radome to the airframe is also a critical mechanical design problem in high temperature applications. The high aerodynamic loads produce large bending moments which often occur at the end of the missile flight and after expose to significant heating. For this reason the bonding, fasteners and clamps must be designed correctly [4].

2.1.2 Electrical Design Considerations

The electrical performance of any radome-enclosed antenna is altered due to the presence of a radome. This change in performance is due to the distortion of the EM fields near the antenna which are caused by interactions at the material interface, and amplitude, phase and polarisation changes due to the dielectric material of the radome. The distorted radiation pattern includes changes in gain, sidelobe levels, beamwidth, null depth and polarisation characteristics.

According to [3], the major parameters on which the radomes EM energy is dependant are:

- Frequency
- Radome wall construction
- Incident angle of the EM wave
- Polarisation of the incident EM wave

The radome designer has little control of three of the parameters mentioned above. The radome wall construction, however, is the one parameter where the designer has a larger amount of control.

2.1.2.1 Radome wall design approach

An ideal radome wall design would be a design which has little to no effect on the antenna system requirements whilst still adhering to mechanical and environmental specifications. This situation requires a wall design which would completely transmit an incident EM wave with no reflection or absorption, whilst still maintaining mechanical integrity. This ideal situation is of course not attainable, however, the radome wall can be designed to maximise transmission or minimise reflection, depending on the type of radome required.

To investigate the reflection and transmission properties of a radome wall, a tractable model of the wall is required. Reflection and transmission properties, or coefficients, are not defined suitably for curved surfaces. The curved surface however, can be modelled using a plane sheet or slab for an approximate analysis, provided that the radius of curvature is electrically large. A further approximation is to model the complex field distribution of the antenna, which provides the incident EM wave, as a plane wave of uniform amplitude. The design problem is thus reduced to the investigation of transmission and reflection coefficients of an infinite plane sheet penetrated by an incident plane wave. This method has long been applied in radome design and analysis [5].

The conditions for a plane wave incident on an infinite, uniform thickness, dielectric slab are shown in Figure 2.4. The incident angle, θ_i, is the angle between the vector pointing towards the source of the plane wave, $-\hat{k}$, and the dielectric surface normal, $\hat{n}$. The *plane of incidence* is defined as the plane containing $\hat{k}$ and $\hat{n}$. The polarisation of the incident plane wave is referenced to the plane of incidence as follows: parallel polarisation (TM) occurs when the incident field has components in the plane of incidence whilst perpendicular polarisation (TE) occurs when the field components are perpendicular to the plane of incidence. These references are significant because, for an isotropic material, TM polarised incidence results in TM polarised reflection and transmission, and likewise for the TE polarisation. [4]

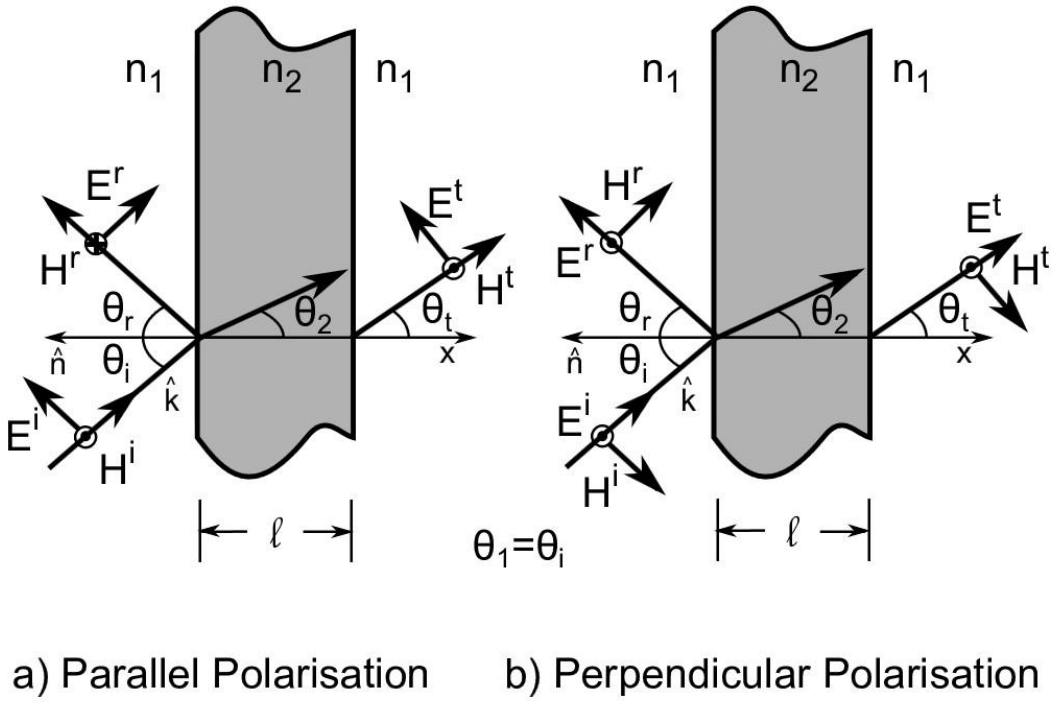

Figure 2.4: Conventions used for plane-wave propagation through a dielectric slab

A discontinuity between two media, that is the transition from one medium to another, causes the reflection of an EM wave. A single dielectric slab has two such discontinuities and will therefore have a pair of reflections. The overall reflection of a radome wall is the superposition of the individual reflections; where its magnitude is determined by the magnitudes and phases of the individual reflections. Overall reflections can be reduced (overall transmission increased) by either

reducing each of the individual reflections or by adjusting the spacing between each discontinuity to obtain partial or complete phase cancellation. [5]

The fields present inside the dielectric slab are a combination of the backward- and forward-traveling waves produced by the reflections at each material discontinuity or interface. From Maxwell's equations, the boundary conditions require a continuity of the tangential electric and magnetic components at all material interfaces. Therefore, analysis can be based on the transverse field components and their relationship between adjacent boundaries.

These fields and dielectric slabs are analogous to cascade TEM transmission lines, where the ABCD transmission matrix used for microwave circuits [6] can also be used to describe the reflection and transmission properties of the dielectric slabs. The ABCD formulation models a layer (dielectric slab) as a two-port network with its own unique ABCD matrix, an input and an output. This allows multi-layered structures to be solved by having the output of one layer becoming the input to the next layer and so on. The ABCD matrices of each individual layer can be cascaded in a matrix product to obtain the overall transmission and reflection coefficients of all the layers as seen in Figure 2.5 below.

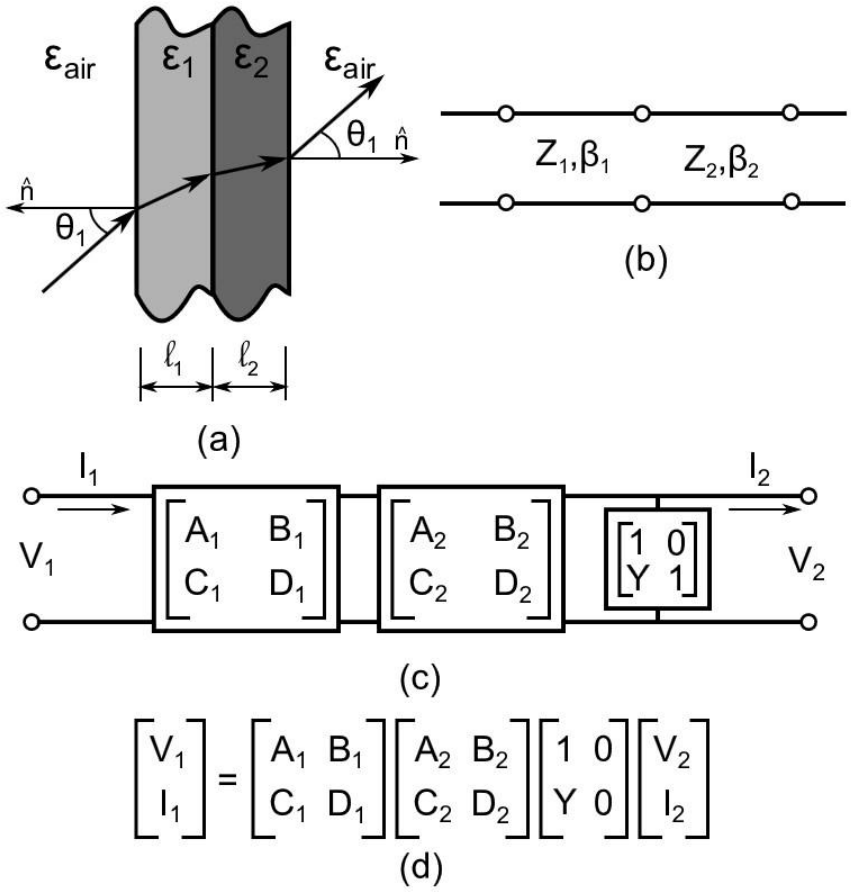

Figure 2.5: (a) Multi-layer radome wall; (b) transmission line model; (c) cascade connection of the ABCD matrix two-port networks; (d) cascade ABCD matrix used in the solution.

Considering the single slab of Figure 2.4, the transverse components of the total fields at the input side consist of incident and reflected fields, $E_t^i(1+\Gamma)$ and $H_t^i(1-\Gamma)$, and are related to the transverse components on the output side, E_t^t and H_t^t, by Eq. 2.9.

$$\begin{bmatrix} E_t^i(1+\Gamma) \\ H_t^i(1-\Gamma) \end{bmatrix} = \begin{bmatrix} A & B \\ C & D \end{bmatrix} \begin{bmatrix} E_t^t \\ H_t^t \end{bmatrix} \qquad 2.9$$

The formulas for the ABCD parameters presented in [6] are for an ideal transmission line and can be used when the angle of incidence is zero. Another model called the *transverse transmission line model* is an adapted version of the above which considers all angles of incidence ($-90 < \theta_i < 90$) and is usually used for radome analysis where the angle of incidence is rarely zero. When an

oblique angle of incidence is present, reflection and refraction at the layer interface takes place which obey the well-known Snell's Laws [7]. The two laws of *reflection* are given as:

- The incident ray, the reflected ray, and the normal to the reflecting surface at the point of reflection lie in the same plane.
- The incident and reflected rays make equal angles with the surface normal.

Snell's Law of *refraction* predicts how the incident angle changes when moving from one media to another by

$$n_1 \, sin(\theta_1) = n_2 sin(\theta_2) \qquad 2.10$$

where n_1 and n_2 are the indices of refraction of the two media, θ_1 is the incident (θ_i) and θ_2 is the refracted angle, respectively. The rule of thumb is a wave moving from a less dense to a more dense medium will bend towards the surface normal and vice versa.

Analogous to an ideal transmission line, each medium has a characteristic or intrinsic impedance given by

$$Z_n = \frac{120\pi}{\sqrt{\varepsilon_n}} \qquad 2.11$$

where $120\pi \approx 377\Omega$ which is the impedance of free-space and ε_n is the relative permittivity of layer n. The ABCD matrix for the dielectric wall now looks as follows

$$\begin{bmatrix} A & B \\ C & D \end{bmatrix} = \begin{bmatrix} cos(\beta l) & jZ_o sin(\beta l) \\ jY_o sin(\beta l) & cos(\beta l) \end{bmatrix} \qquad 2.12$$

where l is the slab thickness, and

$\beta = \frac{2\pi}{\lambda}\sqrt{\varepsilon_n}\cos(\theta_i)$ (the propagation constant)

$Z_o = Z_n \cos(\theta_i)$ (for parallel or TM polarisation)

$Z_o = Z_n / \cos(\theta_i)$ (for perpendicular or TE polarisation)

$Y_o = 1/Z_o$ (the admittance)

The dielectric slabs transmission coefficient, $T = E^t/E^i$, and reflection coefficient, $\Gamma = E^r/E^i$, are given by Eq. 2.13 and Eq. 2.14 respectively, where Z_o is the transverse impedance which differs with polarisation, as stated above.

$$T = \frac{2}{A + B/Z_o + CZ_o + D} \tag{2.13}$$

$$\Gamma = \frac{A + B/Z_o - CZ_o - D}{A + B/Z_o + CZ_o + D} \tag{2.14}$$

The phase of T is calculated to the output side of the slab. The phase shift introduced by the insertion of a slab into the propagation path is an important parameter in radome design. The *insertion phase*, IP, is obtained by removing the free space phase shift from the input to the output and is given by

$$IP = \angle T + \frac{2\pi}{\lambda} t cos\theta_i \tag{2.15}$$

The phase of T is adjusted by the IP to obtain the insertion transmission coefficient. Insertion phase can be a strong function of polarisation and incidence angle, which for highly curved radome, leads to a distortion of the transmitted wave front and cause bore sight error and cross polarisation on the antenna. [4]

2.1.2.2 Radome wall configurations

The radome wall configuration is designed so that the mechanical, electrical and environmental design considerations are met using available materials and constructing techniques. This section will briefly discuss the most common radome wall configurations together with their electrical characteristics. Figure 2.6 shows the wall types which are discussed.

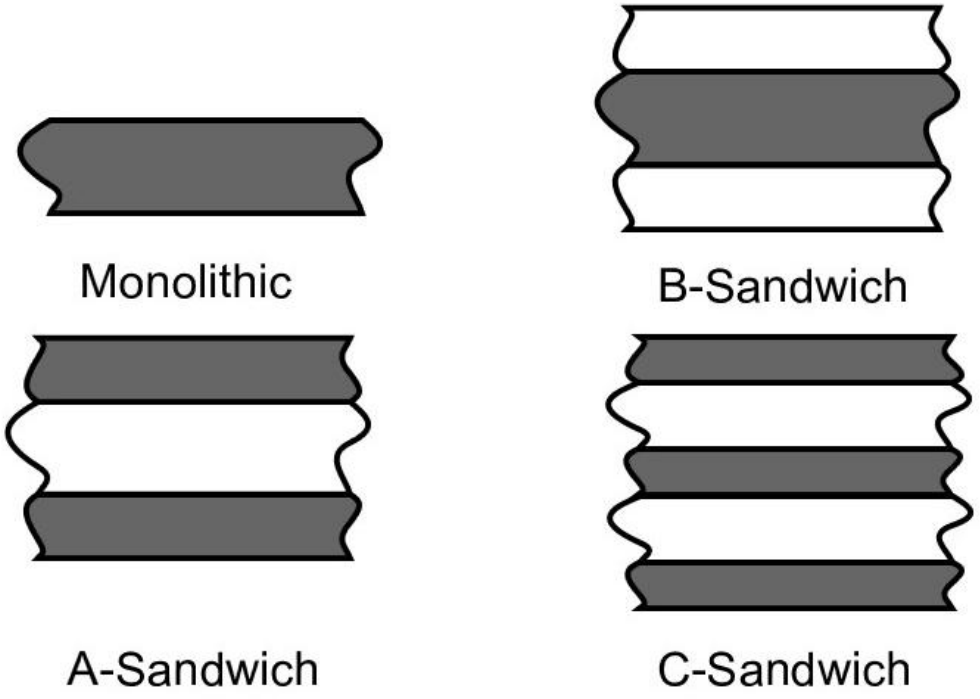

Figure 2.6: Radome wall-constructions (modified from [4])

The most simple wall configuration is the monolithic or single wall type and consists of a single, uniform thickness slab of homogeneous dielectric material. The electrical thickness of the slab may vary from integer multiples of ½ λ in the dielectric medium (λ_m) to very thin (less than 0.1 λ). Thin wall designs are attractive at longer wavelengths where small values of δ/λ (δ is the construction tolerance) can be realised with a wall that has adequate strength and rigidity. Multiple half wave designs are used at higher frequencies where structural design specifications restrict thin wall designs.

According to [8] the multiple half wavelength designs are characterised by narrowband (6-10% [4]) high fineness ratio radomes operating at high speeds with low loss, low bore sight error and slope, and low sidelobe level degradation. The half wavelength properties are such that the insertion phase difference (IPD) variation with incident angle and polarisation lead to low bore sight error characteristics. These conditions occur at wall thicknesses close to optimum transmission/minimum reflection given by Eq. 2.16 where the order of the radome wall is n and θ_d is the design angle.

$$d = \frac{n\lambda}{2\sqrt{\varepsilon_r - sin^2\theta_d}}, \qquad n = 1,2,3,\ldots \tag{2.16}$$

Shipboard and ground-based applications often use monolithic radomes due to ease of design and little to no weight restrictions. Half- and full-wave monolithic walls are also common in high-speed airborne radomes, whilst lighter sandwich configurations are often used for lower-speed aircraft and missile applications. [4]

Sandwich or multilayer configurations are used when the mechanical and electrical properties of the monolithic design are unacceptable for the intended application. The most common multilayer configurations are discussed next, namely the A sandwich, B sandwich and C sandwich.

The A sandwich configuration is the most basic and consists of three layers: two outer high strength skins separated by a lower-density, lower-dielectric core material which is typically made of foam or honeycomb. This wall configuration has a greater strength-to-weight ratio than the monolithic configuration of the same weight, which is useful depending on the application.

The A sandwich design process starts by selecting the outer skins thicknesses. The core thickness is then chosen so that the reflected wave from the second skin cancels the reflected wave from the first skin at the desired frequency and angle of incidence. This wall configuration is used in many narrowband, blunt-nose radomes where low incidence angles provide nearly uniform transmission properties. This configuration is also used in wideband applications such as streamlined missile radomes. [4]

According to [8], there are a number of weaknesses in the A sandwich design. Firstly, the insertion phase relationships with a changing incidence angle and polarisation are not as attractive as the half wavelength monolithic slab leading to poor bore sight error performance. Secondly, the sandwich structure provides a poor substrate for erosion protection materials and consequently fails more often than the half wave monolithic wall. Other disadvantages include poor electrical strength, lightning protection degrading the electrical performance due to the large number of diverter strips needed and finally, a wall structure which offers virtually no resistance to bird or hail impact.

The B sandwich configuration is the reverse of the A sandwich with a dense core material and two lower-density outer materials, which can serve as quarter wave matching layers. The B sandwich

can provide very wide bandwidth at high incidence angles. The B sandwich however, has limited structural and environmental properties due to the lower-density outer layers, which severely limit the applications for which it can be used. [4]

The C sandwich consists of five layers, similar to two A sandwiches joined together, which will provide greater strength and rigidity than the other two sandwich configurations and provide more degrees of freedom for the electrical design. According to [9] and [10] a good transmission match can be obtained independent of the insertion phase which enables the design of highly curved radomes using varying thicknesses to obtain uniform amplitude and phase transmission characteristics.

Other radome configurations not discussed here are metal-loaded, space-frame and grooved radome. More information on these configurations together with references are available in [4].

2.1.2.3 Radome Bore Sight Error (BSE)

Radome bore sight error can be described as the difference between the angular position of a distant reflecting object measured using a radar with an enclosed antenna and the position of the reflecting object measured by the antenna without a radome present [11]. The radome is responsible for the changes in electrical performance of the receiving antenna due to the following factors: (1) dissipative losses within the walls dielectric material, (2) electrical phase shift (IP) introduced by the presence of the radome and (3) internal reflections [12]. *Bore sight error* (BSE) and *radome bore sight error slope* (BSES) are two of these changes to the antennas electrical performance. BSES is defined as the rate of change of the BSE with respect to antenna scan angle. A visual representation of BSE is shown in Figure 2.7 below.

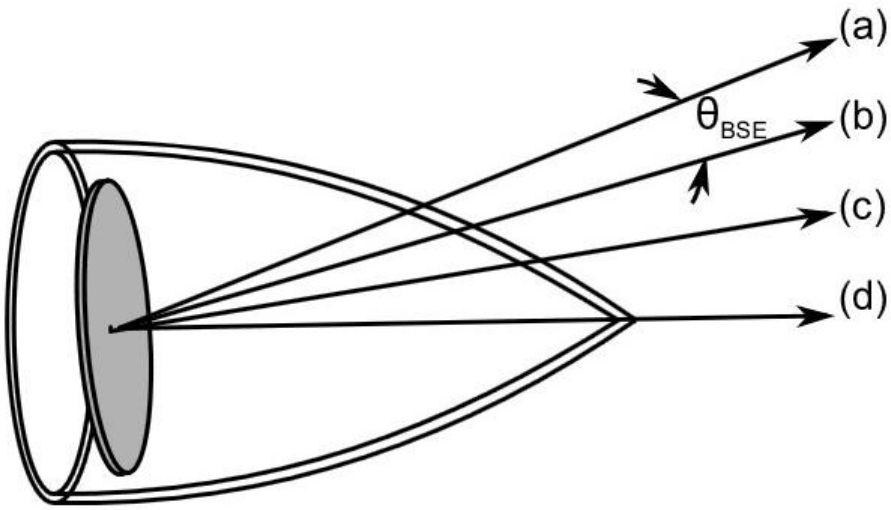

(a) Apparent line-of-sight (with radome)
(b) Actual line-of-sight (without radome)
(c) Antenna centreline
(d) Radome centreline
(θ_{BSE}) Angular boresight error

Figure 2.7: Visual representation of BSE.

A guidance antenna system is needed for BSE and BSES calculations. One of the most commonly used antennas are monopulse antennas. The term monopulse refers to a signal processing technique in which only a single radar return pulse is needed to resolve a targets location in both the elevation and azimuth planes of the antenna. [12]

There are several methods by which a monopulse angle measurement can be made, but for brevity only the amplitude-comparison will be discussed through the use of Figure 2.8.

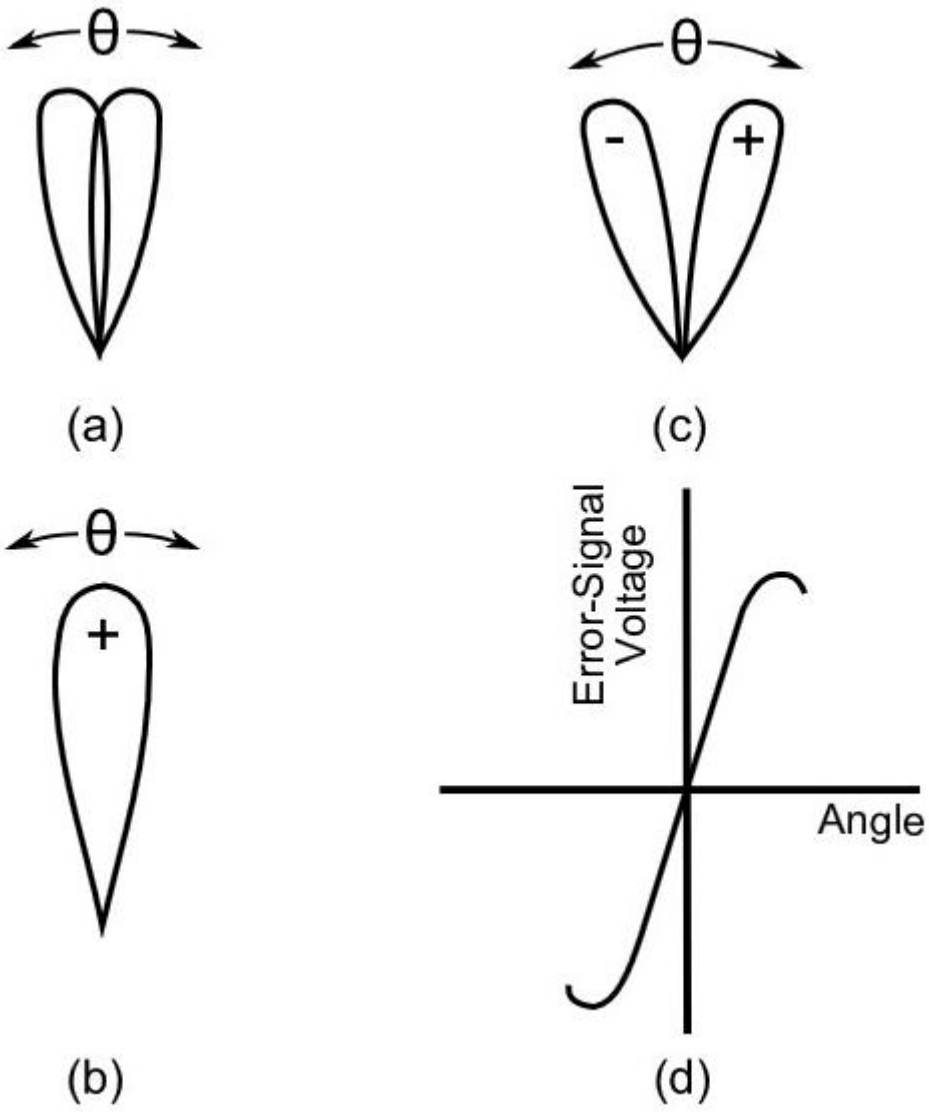

Figure 2.8: Monopulse antenna patterns and error signal. (a) two squinted antenna beams; (b) sum pattern of the two squinted beams; (c) difference pattern; (d) error signal (modified from [13])

The amplitude-comparison monopulse employs two overlapping antenna patterns to obtain the angular error in one co-ordinate (Figure 2.8 a). These overlapping antenna patterns can be generated by a single reflector or with a lens antenna illuminated by two adjacent feeds. Error signals in both the azimuth- and elevation can be obtained by using a cluster of four feeds. The sum and the difference of the two antenna patterns are shown in Figure 2.8 b and Figure 2.8 c respectively. The sum pattern is used on transmission, while both the sum and the difference patterns are used on reception. The signal received with the difference pattern provides the

magnitude of the angle error. The direction of the angle error is found by comparing the phase of the difference signal with the phase of the sum signal. The signals received from the sum and difference patterns are amplified separately and combined in a phase-sensitive detector to produce the angle-error signal, shown in Figure 2.8 d. [13]

A more comprehensive look at tracking radar systems is available in [13] and will not be discussed here. The methods used for the monopulse tracking and BSE calculations will be described in more detail in the relevant chapters to come.

2.1.3 Environmental Design Considerations

The radome environment is dependent on the application for which it is designed and is one of the primary factors in determining the shape, material and radome wall design.

The important environmental factor for ground-based radomes is wind loading. Humidity, blowing dust or sand, ice, rain, hail, snow and moisture build-up on the outer wall must all be considered. The radome mounting must also be designed to be able to survive these harsh conditions. [4]

Airborne radome designs are primarily driven by aerodynamic loads and the thermal environments. The selected radome configuration must be a trade-off between materials and shape based on vehicle speeds, trajectory, and electrical performance over the elevated temperatures produced by aerodynamic heating [4]. In [14] and [15] a brief introduction to aerodynamic heating is provided, together with a comprehensive number of references on this subject. Non-uniform heating of the radome wall produces a change in electrical performance. The dielectric constant and loss tangent of the wall material can also vary significantly with temperature, thereby changing the transmission properties of the radome.

Rain erosion is a severe problem is missile operation. Radome shape, velocity and material type all influence the degree of rain erosion. Sharp-nose radomes are less susceptible to damage than a blunt-nosed radome because less impact energy is transferred to the structure. Rain erosion manifests itself as pitting on the radome surface and, in extreme cases, may lead to catastrophic failure. The resulting change in radome wall thickness can also cause degradation in the RF performance. Measured data of rain erosion testing conducted on a hemi-ogive radome with a multi-layered wall construction is presented in [3].

Other factors such as water absorption, static electricity and lightning strikes are typical environmental conditions which must be considered in radome design. Factors such as bird or hail

impact are a little more difficult and sometimes impossible to design for. A table presented in [8] summarises, in a reasonably concise way, the major environmental features and the relevant advantages and disadvantages of each. This table will not be reproduced here.

2.2 Radome Analysis Methods

The area of radome analysis is a complex and evolutionary discipline [16]. Early methods were approximate and cumbersome, relying on the use of monograms and other approximations [17]. These approaches used geometric optics for airborne radome analysis but, with the invention of the computer, computer aided design became widespread. Computers allow for more accurate design procedures which are reliable, less prone to errors and simulate relative quickly. The authors of [18] are believed to have published the first paper where a digital computer was used for radome analysis in 1959.

A number of electromagnetic analysis techniques have been derived. Geometric optics (GO) and physical optics (PO) are two techniques which can be easily implemented on a computer [17]. These two techniques are discussed below, with some other techniques summarised thereafter.

2.2.1 Geometric Optics (GO)

The GO technique treats the electromagnetic propagation as light-like in behaviour [17]. This method is particularly suitable for electrically large radome-antenna problems (many wavelengths) but has also shown acceptable results for radomes as small as five wavelengths in diameter.

According to [19] one must consider three aspects when using GO: (1) ray reflections, (2) polarisation and (3) amplitude variations along the ray path and through reflections. GO ray tracing based radome analysis approaches have the following characteristics: (1) conceptual simplicity combined with reasonable accuracy, and (2) application in either transmit or receive modes as shown in Figure 2.9. Accurate and identical BSE predictions have been proven for electrically large radomes in receive and transmit modes [17].

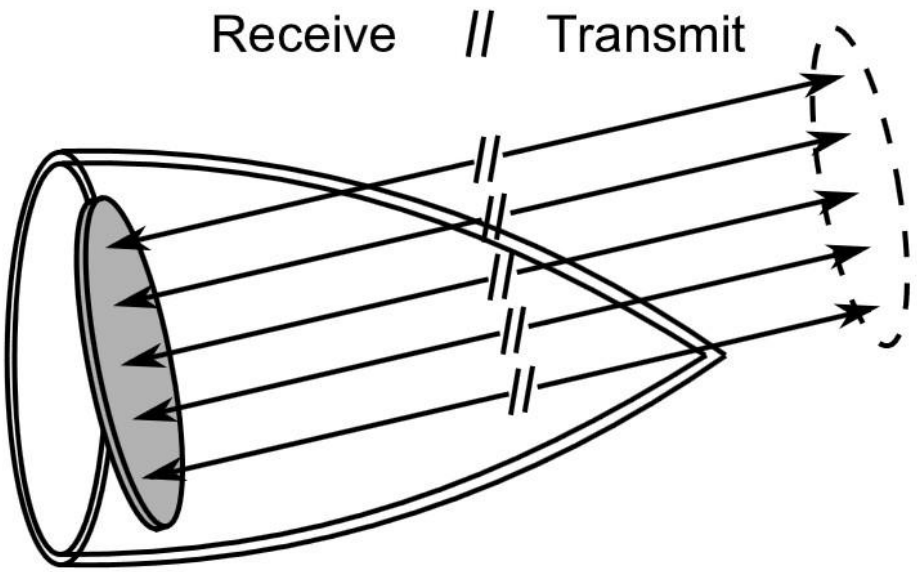

Figure 2.9: GO ray trace approaches.

The receiving formulation determines the voltage at the antenna port when a plane wave is incident on the radome-enclosed antenna. This voltage is obtained from the incident fields and the antenna's characteristics. The real problem that must be addressed is how to calculate the incident fields on the antenna aperture surface. Once determined, these complex fields are used to estimate the BSE of the antenna-radome system. [17]

Assume an incident plane electromagnetic wave originating from an arbitrary but fixed direction, θ and φ. The antenna receive voltage is obtained by integrating the wavefront data over the receive antenna aperture in accordance with the equivalence theorem [11]. Using this theorem, the propagated EM fields are reduced to values on the antenna aperture surface [17].

The received complex voltage at the antenna's terminal is [20]:

$$\iint F^a(E^i T_w)da \qquad 2.17$$

Where: E^i is the incident plane wave function

F^a is the complex valued aperture distribution at a point on the antenna surface

T_w is the complex valued transmission coefficient at the ray-radome intercept point

This integration extends over the physical antenna surface area for which F^a has a significant contribution. F^a can be found from probing the near field at several wavelengths from an actual antenna surface and applying the Fourier transform technique [20]. The complex transmission coefficient, T_w , and the incident plane wave function, E^i , will be described in Chapter 3.

The transmit GO formulation assumes a known antenna aperture distribution. This distribution is projected through the radome wall to form an equivalent aperture outside the radome. This equivalent aperture distribution includes the effects of the radome wall by modifying the amplitude and phase of each ray using its associated radome transmission coefficients. The points forming the modified aperture distribution are therefore related to the original aperture distribution via [17]:

$$F_{mn}^{a\prime} = T_w F_{mn}^{a} \qquad 2.18$$

Where: F_{mn}^{a} is the complex valued transmit aperture distribution at point mn on the actual antenna aperture

$F_{mn}^{a\prime}$ is the equivalent aperture distribution

For transmit operation, the equivalent aperture size is the same as the actual antenna aperture size. Assuming the antenna aperture is positioned in the x-y plane and the z axis corresponds to the radome axis, the far-field antenna array pattern can be obtained from the reference plane distribution using Eq. 2.19

$$E_t = \sum_{m=1}^{M}\sum_{n=1}^{N} F_{mn}^{a\prime} e^{-jk(x_m \sin\theta\cos\varphi + y_n \sin\theta\sin\varphi)} \qquad 2.19$$

where $x_m = md_x$, $y_n = nd_y$, and d_x, d_y are the sample spacing in the x- and y- coordinate directions, respectively.

2.2.2 Physical Optics (PO)

The PO technique is based on Huygens' Principle, which states that each point on a primary wave front can be considered as a new source of secondary spherical waves and that a secondary wave front can be constructed as the envelope of these spherical waves. Figure 2.10 illustrates that a

spherical wave from a point sources propagates as a spherical wave whilst a plane wave continues as a plane wave. In the PO technique the primary assumption is that currents used to model the structure radiate as if the structure is locally planar. Surface integration formulations employ PO methods producing reasonably good results for radome-enclosed antennas that are electrically small (smaller than a wavelength). [17]

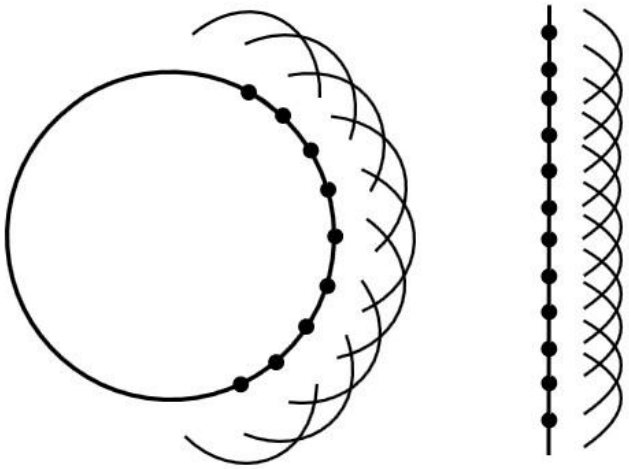

Figure 2.10: Huygens' sources: (left) point source and (right) plane wave [17]

According to [17] the assumptions made in GO techniques cause PO techniques to offer higher computational accuracy. One such assumption is that the electromagnetic wave propagates as a plane wave confined to a cylinder whose cross section defines the antennas aperture. As with the GO, PO too can work in both receive and transmit modes. These two modes of operation will be summarised next.

As previously stated, the GO approach is acceptable for radomes with a diameter of some five wavelengths or more. Diameters smaller than this require too many approximations, thereby making the use of PO preferable. By integrating over the radome's surface using the Kirchhoff-Fresnel integral yields better results in obtaining the fields at each point on the antenna aperture than the GO techniques. An external reference plane is necessary to accomplish this integration. This reference plane is used to reformulate the incident plane wave as a grid of Huygens' sources. Rays are then traced between this grid and each point in the antenna aperture as depicted in Figure 2.11 and solved by Eq. 2.20. [17].

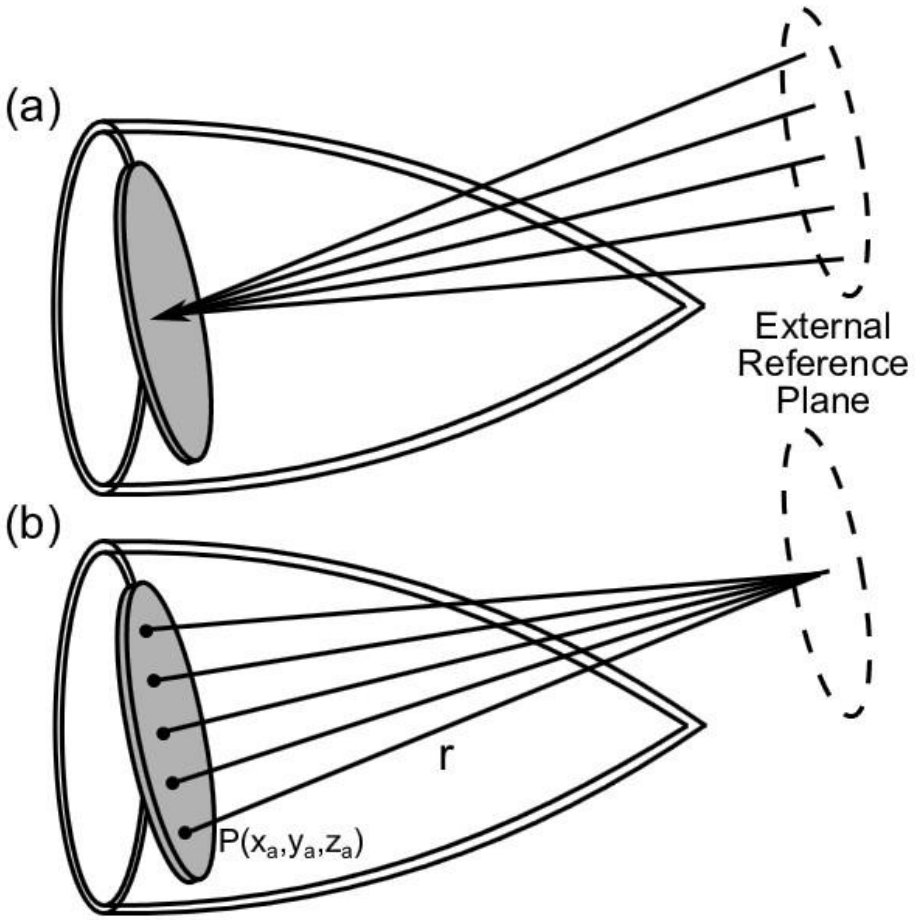

Figure 2.11: Physical optics: (a) receive and (b) transmit

$$V_a = \iint F^a \left(\iint E^i T_w \frac{e^{-jkr}}{r} ds \right) da \qquad 2.20$$

The outer integration extends over the antenna surface area for which F^a has a significant contribution, and the inner integration is over the external reference plane where k is the wave number ($2\pi/\lambda$) and r is the distance from each point on the external reference plane to an antenna aperture point, (x_a,y_a,z_a).

The primary difference between direct ray (GO) and surface integration (PO) methods is in the computation of the total transmission coefficient. Both use the flat plate (slab) approximation of the radome wall at the ray-radome intercept points and both ignore multiple internal reflections

and trapped waves. The PO method, however, uses the integration of a bundle of rays through the radome wall which creates a denser sampling of the radome curvature variations, resulting in a more robust wall transmission model. The GO and PO receive ray trace methods have been compared with measured data in [17] via [20]. The overall consensus is that the surface integration technique was more accurate, especially for radomes that were small in wavelengths.

The transmit PO formulation consists of the following steps:

- Determine the antenna near-field distribution on the inner surface of the radome
- Calculate the transmission coefficients of the radome wall and apply them to the near-field distributions to give the field on the exterior of the radome
- Transform this exterior field to the far field using the Fourier transform technique

The PO transmit equations below assume that each point on the antennas aperture radiates as a Huygens' source. The complex distribution for each point on an external reference plane can be derived via [17]:

$$F_{mn}^{a\prime} = \iint F^a T_w \frac{e^{-jkr}}{r} da \qquad 2.21$$

Once again the integration extends over the physical antenna surface area for which F^a has a significant contribution and $F_{mn}^{a\prime}$ is the complex valued transmit aperture distribution at a point on the external reference plane surface.

This solution requires the area of the external reference plane to be roughly two to four times the physical area of the antenna. An exact solution corresponds to an infinite external plane, which is not possible. The far-field antenna array pattern can now be computed using Eq. 2.19.

The CADDRAD code implemented by [21] is a good example of the use of PO in radar/radome analysis. CADDRAD works in the transmit ray-tracing method, which from the above discussion, will provide more accurate results especially when electrically small radome diameters are used.

2.2.3 Other Techniques

A brief discussion of other techniques used for electrically large radome/radome-antenna problems follows.

Method of Moments (MOM)

A two-dimensional MOM technique was applied by [17] via [22] to a tangent ogive radome. The dielectric radome was solved by dividing it into mesh cells small enough that the electric field intensity was approximately uniform in each shell. The integral equation for the electric field was then solved.

Another MOM approach was applied by [17] via [23]. Two formulations were used to analyse the electromagnetic fields scattered by a hollow cone. One method used the scalar Green's function and the other a tensor Green's function. The two procedures are equivalent, but differ in the following ways:

- The hollow cone is decomposed differently in the two methods. The tensor Green's function decomposes the cone into spheres, whilst the scalar Green's function decomposes the cone into cylinders, which are subsequently decomposed into angular sectors.
- The cells sizes differ causing the number of cells to differ.
- Polarisation dependence differs.

According to [17], the MOM method is more difficult to apply to radome modelling than the others techniques discussed previously. Little validation and technical data is available to compare the accuracy of MOM when compared to GO or PO methods. MOM however can calculate the effects of guided waves or scattering by a radome rain erosion (conducting metal) tip where GO casts a simple tip shadow onto the antenna aperture.

Plane Wave Spectrum (PWS)

PWS relies on the fact that any radiating field can be represented by a superposition of plane waves in different directions [24]. A discrete PWS is a complex vector array obtained from a Fourier transform of the near-field aperture filed and represents the radiating antenna properties [17].

A three-dimensional method that uses the plane wave spectrum representation to calculate the radiation pattern and BSE for a radome-antenna configuration was developed by [25]. It was shown that the PWS formulation was more efficient in calculating the aperture near fields when compared to other aperture integration methods. The computational times for PWS are

proportional to the aperture diameter, making it a useful advantage for antenna apertures greater than 10 λ in diameter.

In contrast with the PWS analysis, [26] used the modal cylindrical-wave spectrum (CWS) to solve a two-dimensional radome. PWS approximates the dielectric radome locally as a flat dielectric slab, thereby ignoring the radius of curvature. CWS however, approximates the local layer as circular, thereby taking the radius of curvature into account. Another difference between PWS and CWS is that the excitation field in the CWS routine is resolved into a series of modal cylindrical waves.

FDTD Technique

Finite-difference time-domain (FDTD) is a method for solving the differential form of Maxwell's equations. This technique has been applied to radome design as reported by [17] via [27]. The method requires defining a grid over the radome and surrounding space and then applying boundary conditions. The FDTD technique however, can be more computationally intensive than other techniques already described.

Integral Equation Techniques

For electrically large radomes, integral equation methods are also generally impractical because of the enormous computational requirements. However, if the technique is applied to a two-dimensional problem the run times are greatly reduced [17]. The successful application of this technique to a two-dimensional electrically large radome with a high fineness ratio was reported by [28] and [29].

Hybrid PO-MOM

In 2001, [30] developed a hybrid PO-MOM analysis technique for electrically large axis-symmetrical radomes. The procedure combines the MOM formulation, to model the sharp tip region of the dielectric radome, and ray optics in conjunction with PO to model the flatter smoother sections of the radome as shown in Figure 2.12. The radomes considered had a length of almost 100 wavelengths with a diameter of almost 50 wavelengths. The simulation took only 4 hours of simulation time on a 233 MHz computer. This hybrid method reduces simulation time for electrically large radomes and has provided acceptable results.

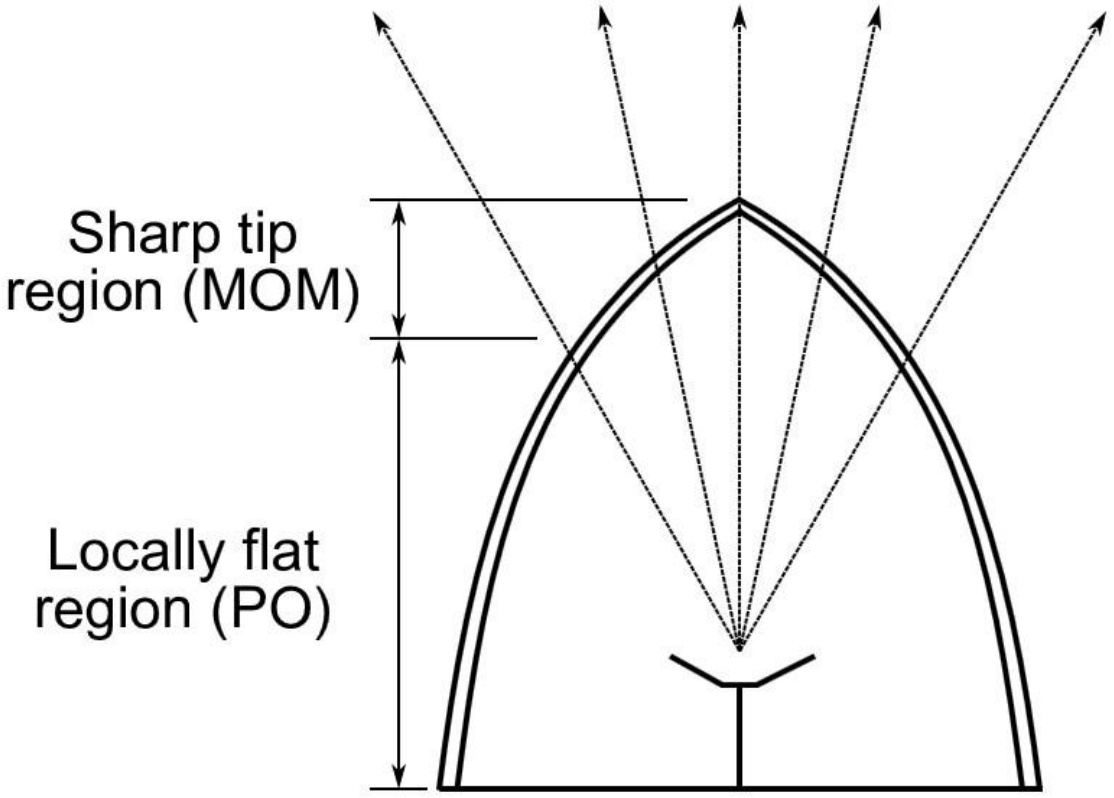

Figure 2.12: Radome geometry and analysis techniques regions (adapted from [30])

3 Radome Modelling

Electromagnetic wave propagation through a curved dielectric shell or radome has been a design problem for many years. The previous section on radome analysis techniques reiterates this due to the fact that there are so many different methods used to solve what is essentially a single problem.

An approximation which many of these techniques use is the modelling of the curved radome as a locally flat, infinite dielectric slab of finite thickness at the position of interest on the radome. The other is to approximate the EM energy incident on the radome as a plane wave. The following chapter will discuss this method of radome modelling.

3.1 Single Infinite Slab

According to [5] there are only three variables needed to analyse a radome wall as a single dielectric slab:

- The angle of incidence of the plane wave
- The dielectric constant of the slab
- The thickness of the slab in wavelengths

These variables, together with the polarisation of the incident plane wave, allow for the setup of a number of design charts which provide virtually all information needed for single radome wall designs.

The transmission and reflection properties of an infinite slab of finite thickness were investigated. This investigation served two purposes: (1) gave insight into the design of a single dielectric slab, and (2) was used to validate the MATLAB code written to model the reflection and transmission

response of a dielectric slab. The 3D electromagnetic software package FEKO[1] was used as the reference to validate the slab's response.

Of the three variables used to define the problem, only the relative permittivity of the material (ε_r) was kept constant. The incident angle of the plane wave varied from 0° to 90° whilst the thickness of the slab was varied from 0.45 to 0.6 wavelengths in the medium. The frequency was in the X-band and the polarisation of the incident plane wave was switched between parallel and perpendicular.

Nearfield monitors, positioned on the upper and lower surface of the dielectric slab, were used in the simulations to measure the E- and H-fields on either side of the slab. The setup is shown in Figure 3.1.

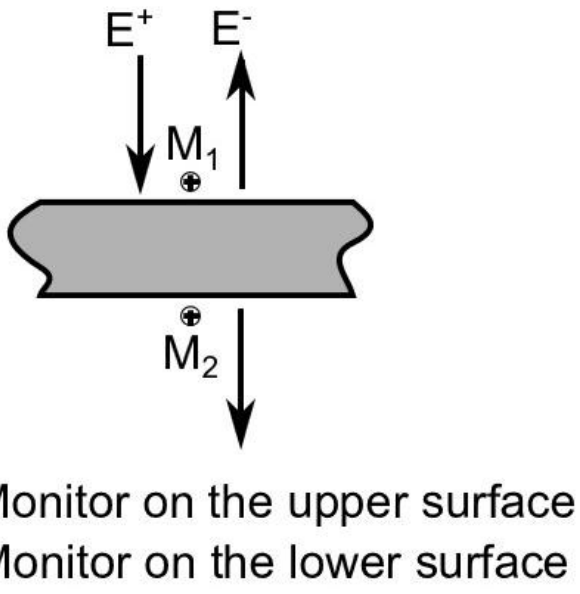

Figure 3.1: Nearfield monitor setup in the FEKO model

The complex E-fields measured by the upper monitor, E_{m1} , is used to calculate the reflection coefficients of the slab as follows:

$$E_{m1} = E^+ + E^- \tag{3.1}$$

$$\Gamma = \frac{E^-}{E^+} \tag{3.2}$$

[1] For more information regarding FEKO, please visit http://www.feko.info/.

Substituting Eq. 3.1 into Eq. 3.2, the reflection coefficient is

$$\Gamma = \frac{E_{m1}}{E^{+}} - 1 \tag{3.3}$$

The transmission coefficient is simply the complex E-fields measured by the lower nearfield monitor, E_{m2}.

Two theoretical methods were used in the MATLAB code. The first is by using the ABCD matrix method mentioned in Chapter 2 whilst the other is through the implementation of Eq. 8.3.1 and 8.4.2 of [31]. These equations are repeated in Eq. 3.4 and Eq. 3.5 for completeness.

$$\Gamma = \frac{\rho(1 - e^{-2j\delta})}{1 - \rho^2 e^{-2j\delta}} \tag{3.4}$$

$$T = \frac{(1 - \rho^2)e^{-j\delta}}{1 - \rho^2 e^{-2j\delta}} \tag{3.5}$$

Where $\delta = \beta l$ from Eq. 2.12 and $\rho = (Z_L - Z_o)/(Z_L + Z_o)$. Z_L and Z_o are both depend on the incident plane waves polarisation and are calculated as follows:

$$\begin{aligned} Z_L &= \frac{120\pi}{\sqrt{\varepsilon_r}} cos\theta_2 \ (for\ parallel\ polarisation) \\ Z_L &= \frac{120\pi}{\sqrt{\varepsilon_r} cos\theta_2} \ (for\ perpendicular\ polarisation) \\ Z_o &= 120\pi cos\theta_1 \ (for\ parallel\ polarisation) \\ Z_o &= \frac{120\pi}{cos\theta_1} \ (for\ perpendicular\ polarisation) \end{aligned} \tag{3.6}$$

θ_1 and θ_2 are the incident and refracted angles calculated using Snell's law in Eq. 2.10.

The comparison between both theoretical methods and the FEKO simulations were identical thus validating the reflection and transmission coefficient calculations which are used in the final radome analysis code. The reflection and transmission results for perpendicular and parallel polarisation are shown in two figures below.

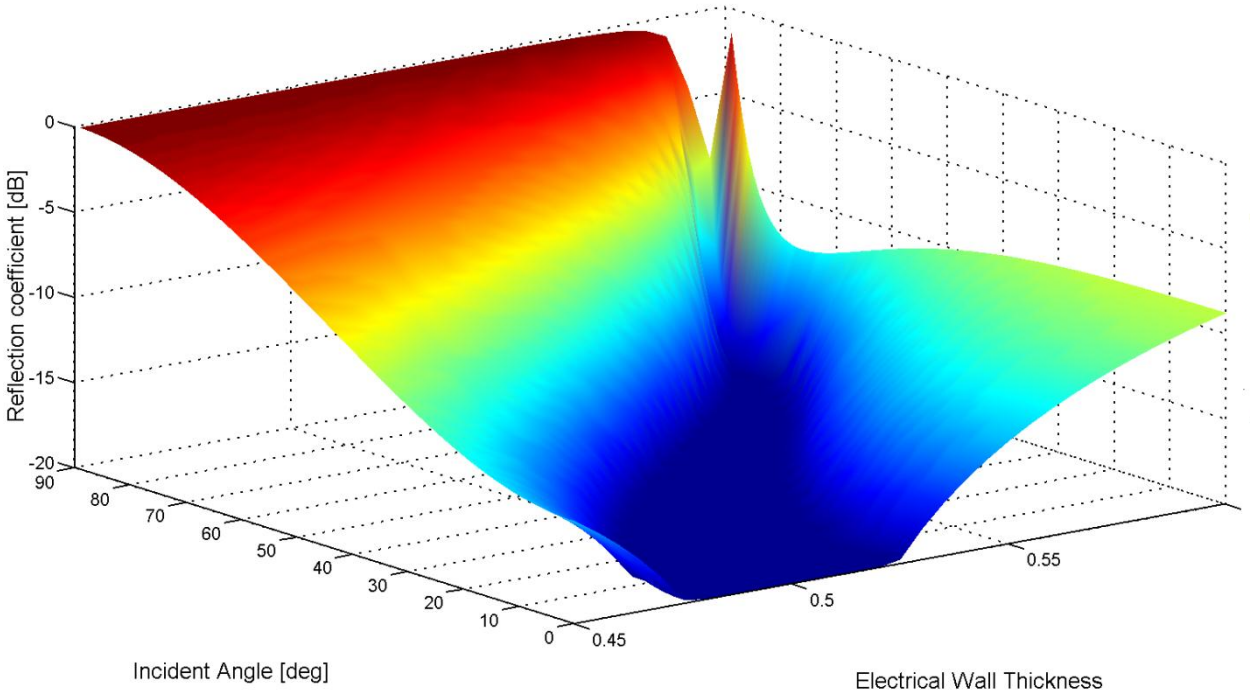

Figure 3.2: TE reflection response.

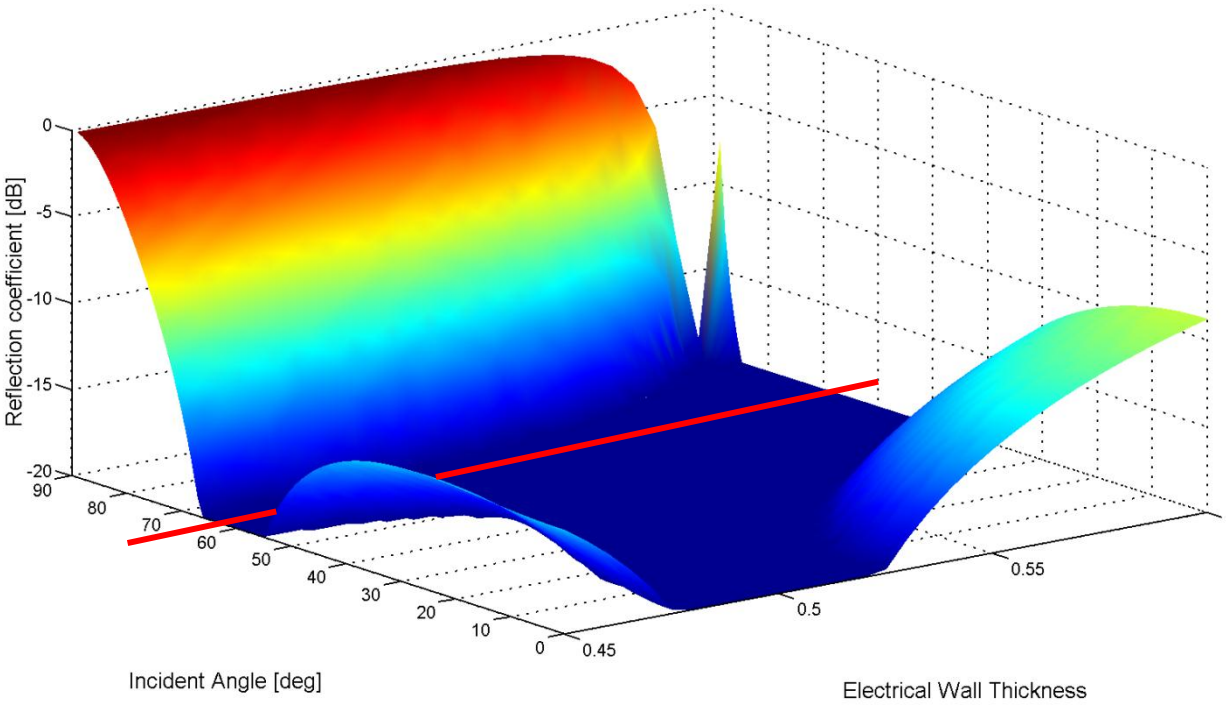

Figure 3.3: TM reflection response.

The reflection and transmission response of a dielectric slab differ remarkably for different incident wave polarisations. At low angles of incidence, $\theta_i < 15^{\circ}$, the results are similar but thereafter the wall thickness required for matching will be different for parallel (TM) and perpendicular (TE) polarisations. Overall the transmission and reflection response of the slab is more attractive for the parallel polarisation. This is due to the Brewster angle phenomena which is present only for this polarisation.

The *Brewster angle*, also called the polarizing angle, is defined as the angle of incidence at which the parallel polarisation reflection coefficient vanishes (this angle is indicated by the red trace in Figure 3.3). At this specific angle, if a mixture of TM and TE polarised waves are incident on a dielectric slab, only the TE or perpendicularly polarised wave will be reflected. [31]

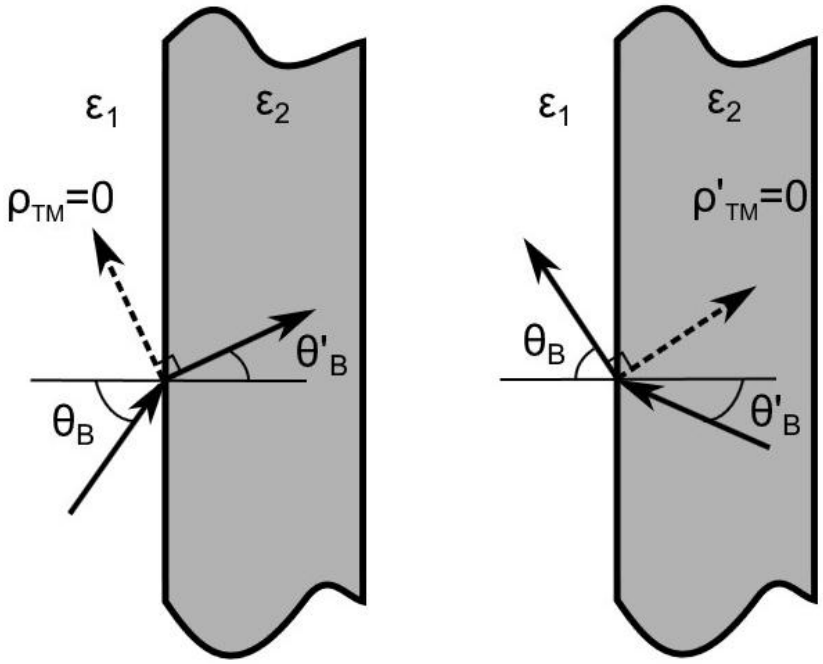

Figure 3.4: Brewster angles

From Figure 3.4, the Brewster angle is calculated as follows:

$$tan\theta_B = \frac{\sqrt{\varepsilon_2}}{\sqrt{\varepsilon_1}} \qquad 3.7$$

Where ε_1 and ε_2 are the relative permittivity's of medium 1 and 2 respectively.

The dielectric wall thickness is usually designed for perpendicular polarisation matching due to the good transmission of the parallel polarisation which is provided by the Brewster angle [4].

3.2 Single Finite Slab – Techniques Investigated

As mentioned previously, many of the design techniques used to solve radome problems model the radome wall as locally flat at the position where the ray intercepts the radome. This assumption however completely ignores the curvature of the radome, which for radomes with a high radius of curvature, can lead to erroneous calculations.

The author conducted a number of investigations to try and quantify the effect of the radius of curvature on the transmission and reflection coefficients. The results of these investigations would be incorporated into the calculations to obtain more accurate results, especially in the highly curved tip region of the radome, however, the investigations conducted were unsuccessful. A briefly summary is given below to prevent any further attempts to solve this problem using these methods.

Replace the infinite slab with a finite slab: This was the initial investigation conducted. If the results of these simulations could be validated against the infinite slab described above, the model and modelling technique are credible. Thereafter the flat slab could be curved, firstly in one direction, and then in another direction creating a doubly curved surface similar to that of a radome.

This relatively simple approach provided problems. The surface equivalence principle (SEP) technique was used to solve the problem and an incident plane wave was used as the excitation for the problem. The length and breadth of the finite slab required adjustment so that the edge effects had a negligible effect on the results. The problem arose that as these parameters were increased, the computational resources and simulation time also increased.

This initial technique was unsuccessful. The slab could not be made large enough to reduce the effects of edge reflections and diffraction, and surface waves (a good review of surface wave topics is found in [32]).

Half a hollow cylinder: This approach was still considered with the hope that the edge and surface wave effects would be reduced due to the curved nature of the problem. An electrically long

dielectric cylinder was created and boundary conditions were set to absorb any trapped energy. Due to the change in incident angle and polarisation, a model which worked for all variations was not achieved. A hollow cone was also used to model the doubly curved radome wall. This approach was also to no avail.

Transient analysis: The cylindrical problems described above were analysed in the time domain. An extra field monitor, positioned on the inside of the cylinder, was used to terminate the simulation once most of the transmitted energy had passed. The results were then converted to the frequency domain using the Fast Fourier Transform (FFT) technique so that a direct comparison could be made with the previous sections results. This technique was also unsuccessful.

Gaussian Beam: The final method worth mentioning was the use of a Gaussian Beam to focus the incident energy on a small area of the finite flat slab. D. Le Roux [33], a support engineer at FEKO, provided a model of the Gaussian Beam which was used to excite the finite slab ([34] shows how this beam can be used to isolate edge scattering from a finite plate). This model constructs a Gaussian Beam from a large number of plane waves. The results however, were once again unsatisfactory.

The results of these techniques could not be used in any way but insight into the modelling intricacies of flat, single and doubly curved dielectric surfaces was obtained.

3.3 Ray Trace Visualisation

In order to gain a basic understanding of the interaction between EM fields transmitted by a radome enclosed antenna, a 2D ray tracing method was written in MATLAB. This method, described next, provided a visual understanding of how the transmitted EM wave propagates from the antennas aperture, through the radome wall and onwards in the intended direction.

Figure 3.5 shows the code flow diagram. Each step will be described next.

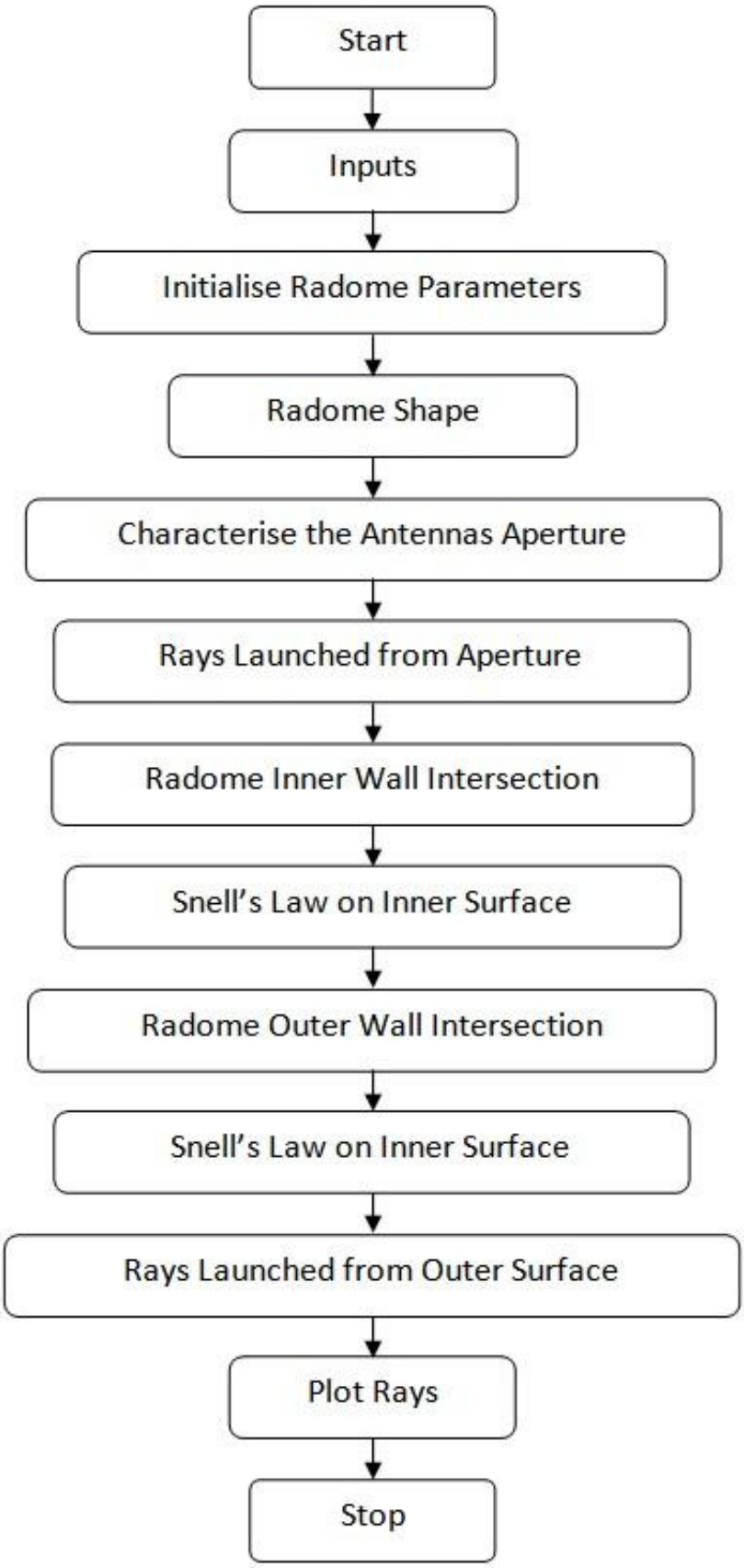

Figure 3.5: Ray trace visualisation code flow diagram

1) Inputs: The system inputs required are:
    a. Radome Profile which can be Tangent Ogive, Power Series (½) or Von Karman.
    b. The angle of the antennas gimbal arm relative to the radome centreline
    c. The number of rays to be traced
2) Initialise Radome Parameters: The following radome parameters are required:
    a. Radome wall thickness
    b. Radome length
    c. Radome base outer diameter
    d. Relative permittivity of the dielectric used
    e. Antenna aperture diameter
    f. Antenna gimbal arm length
3) Radome Shape: The above parameters and inputs are used to determine the inner and outer radome shape. The wall thickness is used as the perpendicular distance between the surfaces along the outer surfaces normal vector.
4) Characterise the Antennas Aperture: The antennas aperture is defined using the inputs and parameters. Mathematical equations of the aperture are setup and are used in the next step.
5) Rays Launched from Aperture: The ray-aperture intersection points are calculated using the antenna aperture equations (step 4) and the number of rays to be traced (step 1). The rays are linearly spaced over the aperture and are launched in the direction normal to the antenna aperture (angle input in step 1). Each ray is described by a unique equation.
6) Radome Inner Wall Intersection: The rays are traced from the antenna aperture towards the radome inner wall. The radome-ray intersection point is calculated by the intersection of two straight lines, those being (1) the ray and (2) the flat slab approximation of the wall at the intersection point. The angle of incidence between the normal of the flat slab and the incident ray is also calculated.
7) Snell's Law on Inner Surface: The angle of refraction is calculated using Snell's Law at the radome-ray intersection point. The dielectric constant (step 1) is used for this calculation.
8) Radome Outer Wall Intersection: The angle of refraction (step 7) is used to trace the ray through the radome wall to the point of intersection with the outer radome surface. The method is the same as that used in step 6.
9) Snell's Law on Outer Surface: Once again Snell's Law is used to determine the angle of refraction from the radome to free-space. This requires a ray moving from a more dense to

a less dense medium, which can lead to the phenomenon called *total internal reflection* if the angle of incidence is larger than the *critical angle* defined by Eq. 3.8 : [31]

$$sin\theta_c = \frac{\sqrt{\varepsilon_1}}{\sqrt{\varepsilon_2}} \qquad \varepsilon_1 < \varepsilon_2 \qquad 3.8$$

When such a ray is encountered, the ray is removed from the calculations and a warning given to the user.

10) Rays Launched from Outer Surface: The angle of refraction is used to launch the rays from the radome outer surface.
11) Plot Rays: This step plots a 2D visualisation of the problem described above. The radome, gimbal arm and antenna aperture surface are plotted first. Thereafter the rays are plotted as they are launched from the antenna aperture, refracted through the radome wall and continue in the intended destination.

The results of four different designs are shown in Figure 3.6 to Figure 3.9. The radome-ray intersection points are indicated by green crosses with the normal to the flat slabs surface indicated by a red trace. The dark green traces indicate the ray's path without the radome whilst the blue traces show the effect which the radome has on the ray's propagation. Table 3.1 shows the inputs and radome parameters used for these designs. The input which was varied was the gimbal arm angle.

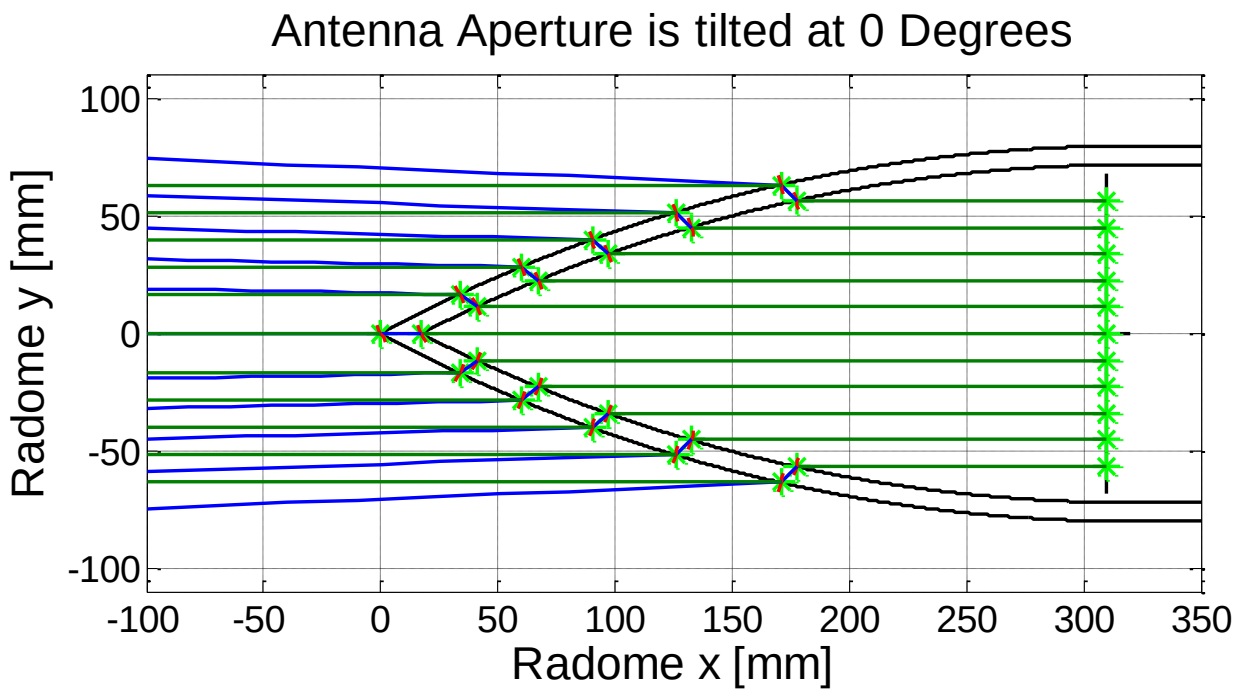

Figure 3.6: Rays launched from an antenna aperture tilted at 0°.

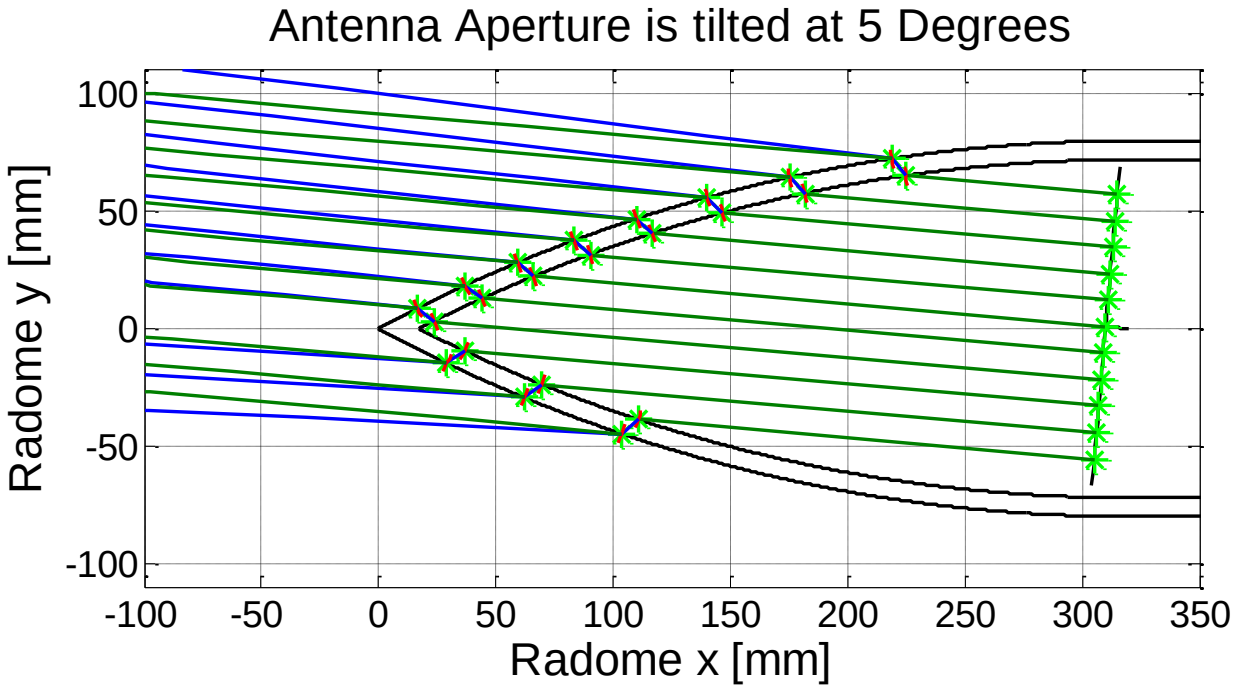

Figure 3.7: Rays launched from an antenna aperture tilted at 5°.

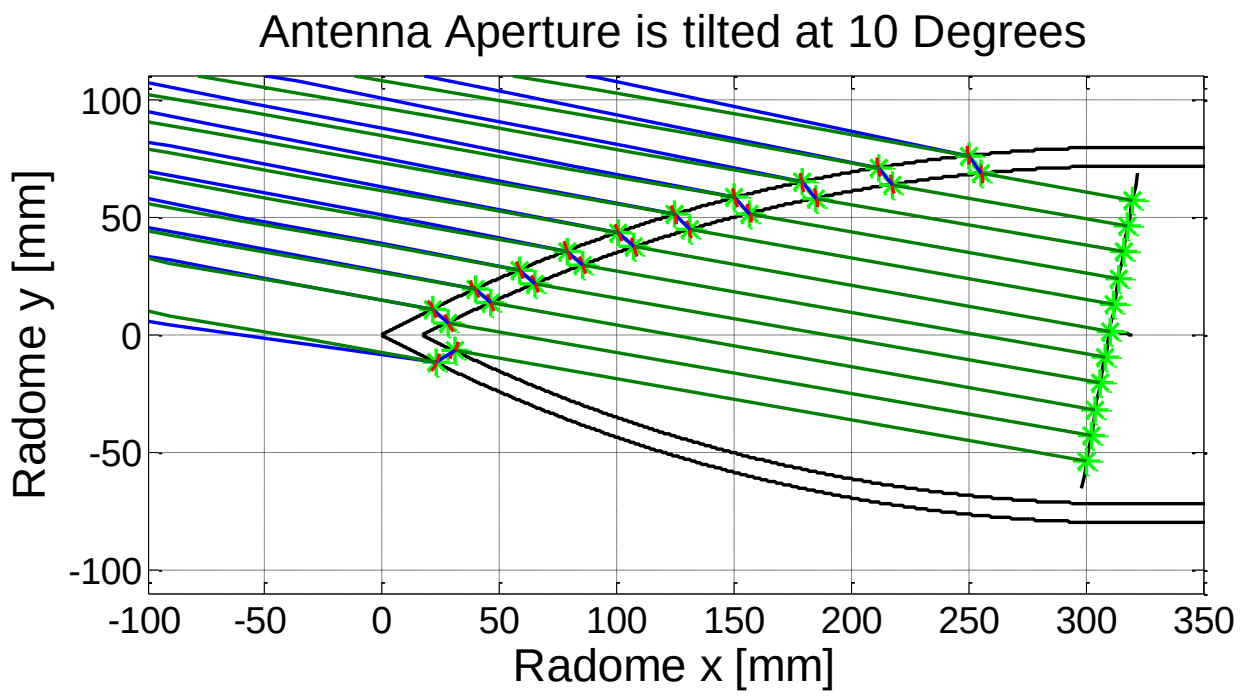

Figure 3.8: Rays launched from an antenna aperture tilted at 10°.

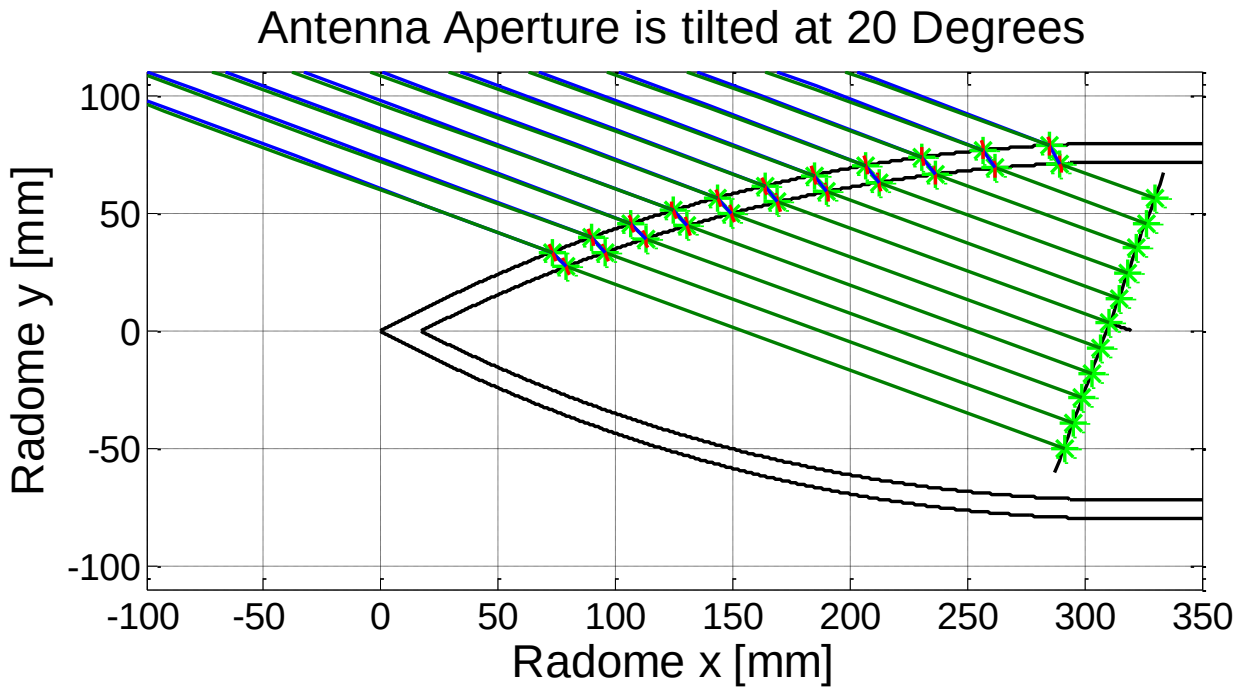

Figure 3.9: Rays launched from an antenna aperture tilted at 20°.

Table 3.1: Inputs to the ray trace visualisation example

Input/Radome Parameter	**Value**	**Unit**
Radome profile	Tangent Ogive	-
Gimbal angles	0, 5, 10, 20	°
Number of rays	11	-
Radome wall thickness	8	mm
Radome length	320	mm
Radome base outer diameter	80	mm
Dielectric relative permittivity	3.5	-
Antenna aperture diameter	68	mm
Antenna gimbal arm	10	mm

The results show that the lower incident angles have greater deviation (blue trace) from the path followed without the radome present (green trace). This is due to the illumination of the sharp tip of the radome where the radius of curvature is small. The tip region, illuminated by rays of low incident angle, has been shown to contribute to radome BSE.

4 Ray Tracing Code

MATLAB code was written to analyse the effect of an electrically large radome on a monopulse antenna system. This Chapter describes the code through the use of flow diagrams and explains each step in the process. Thereafter, the validation of the code against a literature example is discussed. The Chapter is concluded with a discussion of the user interface which was written to make the code more practical and user-friendly.

4.1 Code Flow Diagrams

The *main program's* flow diagram is present in Figure 4.1. This flow diagram consists of four process blocks and a single subroutine. The four process blocks are design inputs to the design problem whilst the subroutine contains the actual methods used in solving the problem.

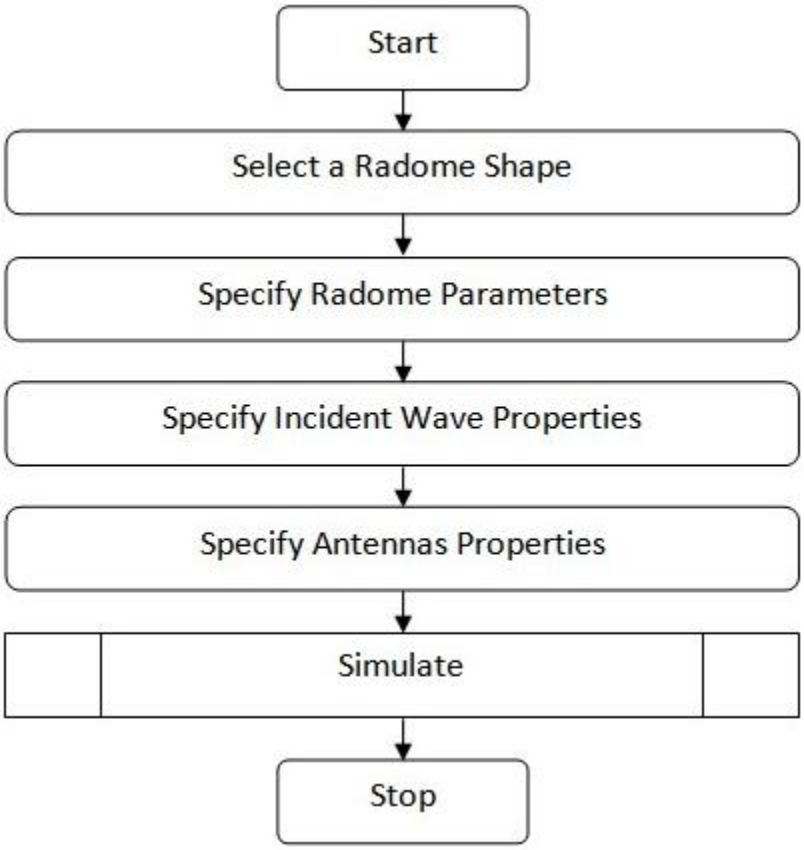

Figure 4.1: Flow diagram for the Main program.

The *simulate subroutine* presented in Figure 4.2 consists of two process blocks, two decision blocks and a single subroutine. The function of the simulate subroutine is to ensure that all the user specified criteria are calculated, and when that has been done successfully, to return the designed outputs to the user. This subroutine contains the main calculation subroutine which traces the rays from outside the radome, through the radome wall and onto the antenna surface. The final step calculates the BSE for the set of input criteria.

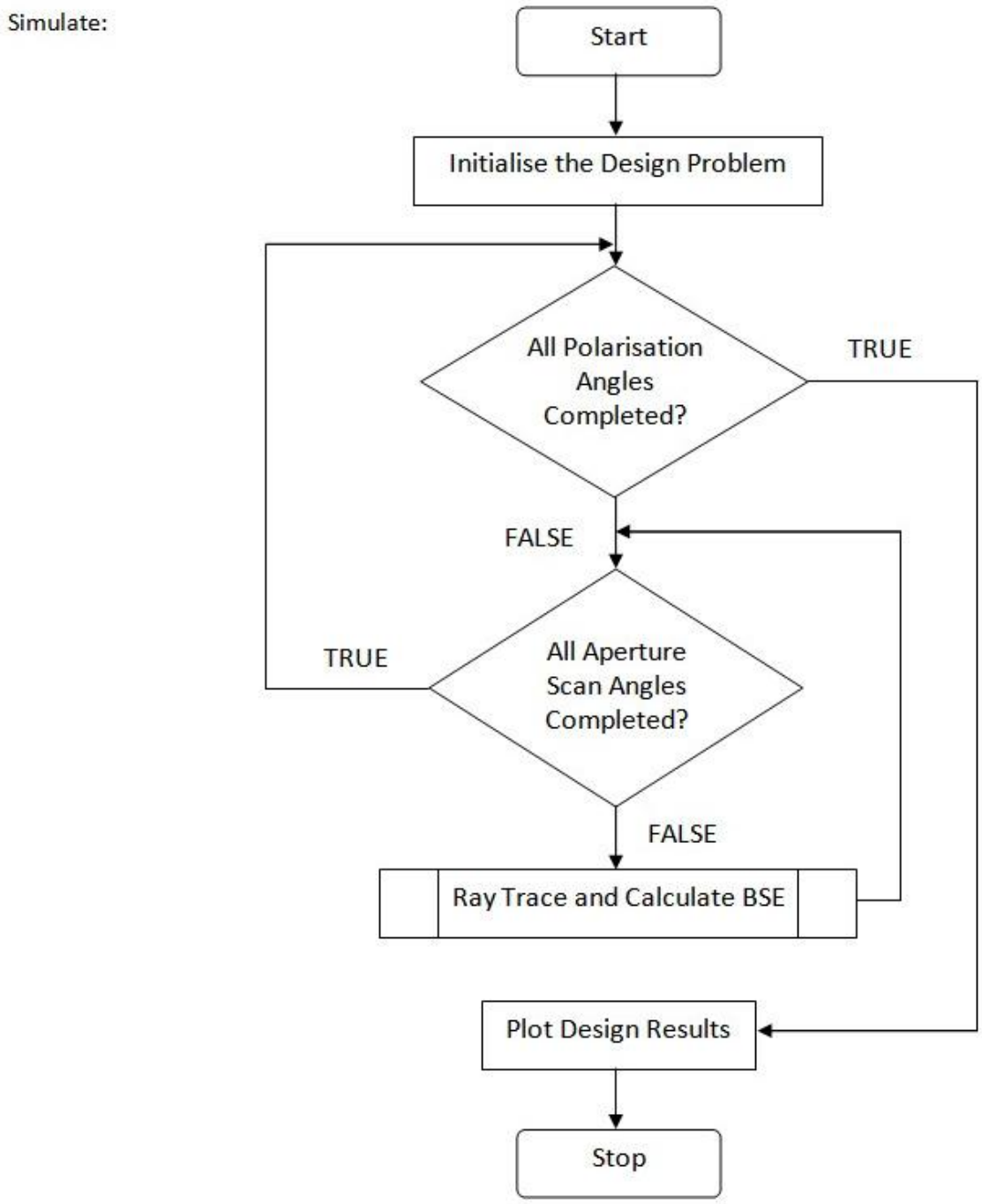

Figure 4.2: Flow diagram of subroutine: Simulate.

Figure 4.3 shows the *ray trace and calculate BSE* subroutine. This can be seen as the core of the design code. This subroutine consists of ten process blocks and a single decision block. This subroutine returns the BSE for the specific set of input parameters.

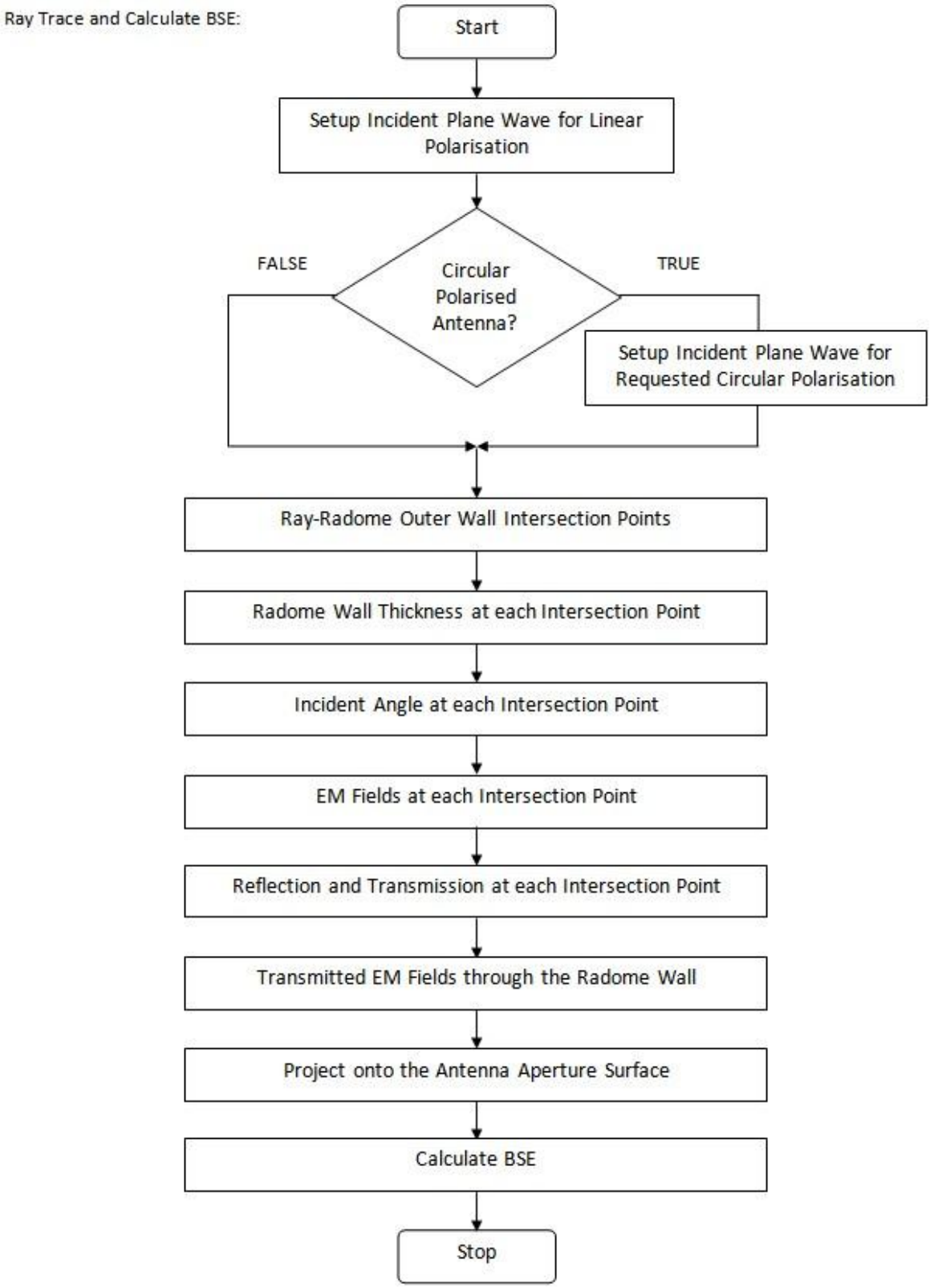

Figure 4.3: Flow diagram of subroutine: Ray trace and calculate BSE.

4.2 Flow Diagrams Explanation

A detailed discussion of the three flow diagrams above follows.

4.2.1 Main Program

The primary function of this flow diagram is to capture all the user input data. This is done by the four process blocks, described below.

Select a Radome Shape: As the blocks title states, the user is required to enter the profile or shape of the radome to be designed. There are three profiles to choose from: (1) Tangent Ogive, (2) Half Power Series or (3) the Von Karman. These radome profiles were discussed, together with their defining equations, in Chapter 2 and will not be repeated here.

Specify Radome Parameters: Table 4.1 below indicates the radome parameters to be specified, along with their units and short names. There are limitations placed on these parameters which are discussed later. Figure 4.4 indicates the radome parameter definitions.

Table 4.1: Radome parameter definitions.

Input/Radome Parameter	**Unit**	**Short Name**
Frequency	GHz	fo
Dielectric relative permittivity		er
Radome wall thickness	mm	t
Radome wall taper	mm	tp
Radome length	mm	lr
Radome base diameter	mm	dr
Antenna pivot position	mm	pl
Antenna aperture radius	mm	ra

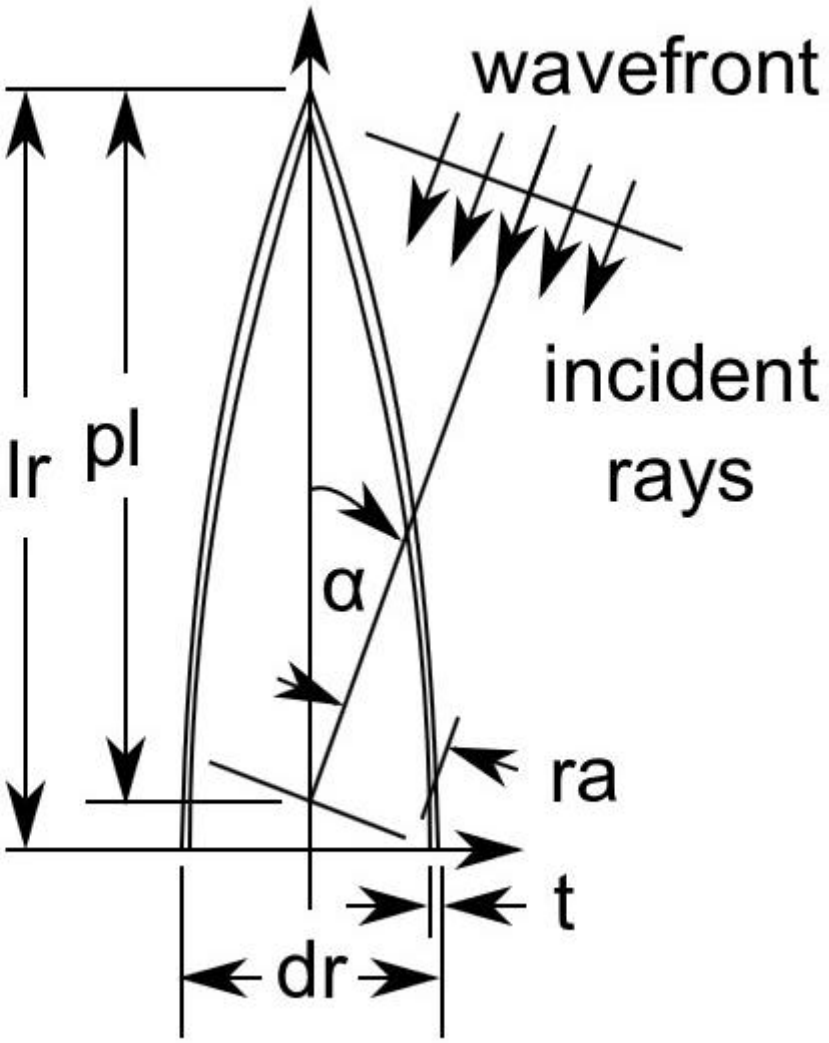

Figure 4.4: Radome parameter definitions.

The only parameter which may be misleading is the “Radome wall taper”. The wall taper is the amount with which the radome wall thickness must vary with respect to the uniform wall thickness at the radome tip. The taper applied here is a linear taper, which starts from the uniform radome wall thickness at the radome base, and tapers linearly towards the nose along the radome length. The wall thickness at the tip is then the uniform radome wall thickness plus the taper, which can have a negative or positive value. Figure 4.5 below illustrates the difference between a tapered wall and a wall with no taper.

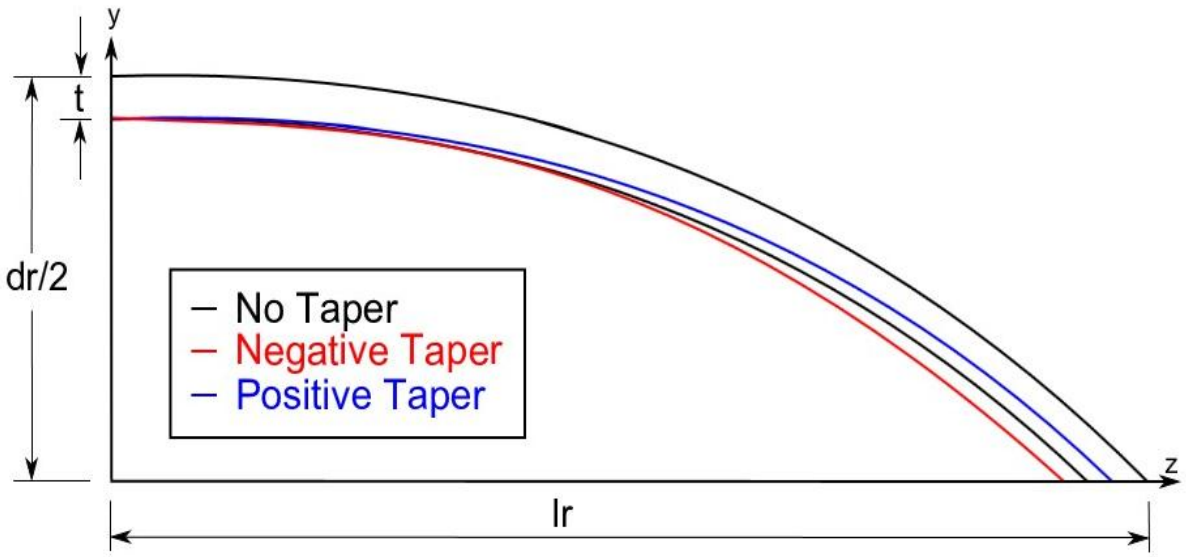

Figure 4.5: Radome wall taper illustration.

Specify Incident Wave Properties: The inputs required for the incident plane wave are the polarisation (φ) and scan angle (α) characteristics. There are two options which the user can select: (1) a single polarisation angle or (2) a range of polarisation angles. When a range of angles is selected, the minimum, maximum and angle increment values must also be specified. Figure 4.6 shows the definitions of the incident plane wave properties, together with other variables, which are used in the equations which follow.

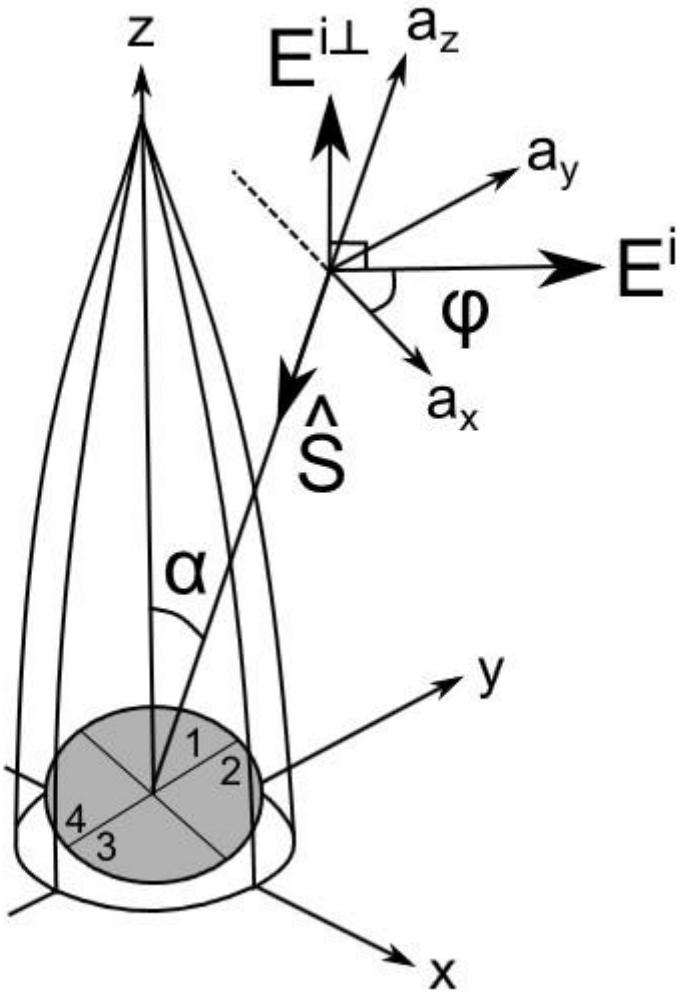

Figure 4.6: Incident plane wave parameter definitions.

Specify Antenna Properties: The first antenna property specified here is the polarisation of the antenna. The three options are (1) linear, (2) right hand circular (RHC) or (3) left hand circular (LHC) polarisation. The other antenna property is the scan angle through which the antenna must rotate. Similar to the polarisation angle, a single value or a range can be specified. Once again a minimum, maximum and angle increment must be specified if a range of scan angles is required.

Simulate: Once all this information has been successfully captured, it is used as the input to the simulate subroutine. This routine has its own flow diagram and will be discussed next.

4.2.2 Simulate Subroutine

The flow diagram of the simulate subroutine is present in Figure 4.2. This subroutine can be regarded as the control routine which determines whether all the simulations have been completed. Once completed the results are presented in a graphical format.

Initialise the Design Problem: This process block uses the radome shape and input parameters to calculate the following:

- *Outer radome profile*: 2D dimensional shape is returned as a matrix of x-y values together with the corresponding normal vector of each point on the outer radome surface
- *Inner radome profile*: The radome wall thickness, wall taper and normal vectors of the outer surface are used to calculate the inner radome matrix of x-y values. The inner surface points are offset from the outer surface points by the wall thickness along each point's normal vector. When a wall taper is specified, the 'tapered resultant wall thicknesses' are first computed along the radome length, and then offset along the normal vector as above.
- Load the standard antenna aperture data provided by K.D. Palmer of Stellenbosch University. The antenna aperture is modelled using symmetrical quadrants, making monopulse tracking possible. The data contains the positions of the aperture points of interest, which scale with aperture radius, as well as data used to calculate the sensitivity of the radome needed for BSE calculations.
- 3D surfaces are created by spinning the inner and outer radome profiles around the radome centreline.

All polarisation Angles Completed? This is a decision block which is used to monitor whether all the user requested polarisations have been simulated or not. If the answer to this query is true, then the ray tracing is complete and the *Plot Design Results* is called. If the answer is false, the next decision block is entered.

All Aperture Scan Angles Completed? This decision block is similar to the one described above. This block, however, monitors the aperture scan angles for a set polarisation value. When the answer to this query is false, the *Ray Trace and Calculate BSE* subroutine is called. The output of this subroutine is then fed to the input of this decision block. Once all the scan angles have be simulated, the program is fed back to the polarisation decision block, thus closing the loop.

Ray Trace and Calculate BSE: As stated already, this subroutine is the core of the ray tracing program. This subroutine will be discussed in detail in the next section.

Plot Design Results: This process block does exactly what its title says. It takes the results of the simulations, that being the BSE for the design, and presents it in a graphical form of 2D traces and/or 3D surfaces.

4.2.3 Ray Trace and calculate BSE

This subroutine is called for every combination of polarisation and scan angle and returns the corresponding BSE. This subroutine consists of ten process blocks with only a single decision block and is present in Figure 4.3.

Setup Incident Plane Wave for Linear Polarisation: The incident plane wave is assumed incident on the outer surface of the radome and is represented by a system of parallel rays with a single ray for every point on the antenna aperture surface. The incident E-field has a magnitude of E_o and changes with polarisation (φ) as follows:

$$E^i = E_o\,[cos(\varphi)\,\boldsymbol{a_x} + sin(\varphi)\,\boldsymbol{a_y} + 0\boldsymbol{a_z}] \qquad 4.1$$

The design decision was made to rotate the radome and keep the aperture in the x-y plane. This was done to simplify the calculations. The results of this simplification is that the plane wave now propagates or has its poynting vector ($\hat{S}$) in the –z direction ($\hat{S} = -\boldsymbol{a_z}$). A further design decision was to set E_o to unity and will therefore be left out of the equations to follow.

Circular Polarised Antenna? This decision is based on the user input under the *Specify Antenna Properties* process block. If the polarisation has been set to either RHC or LHC, then the process block described next is entered. If the answer to this query is false, the flow continues to the *Ray-Radome Outer Wall Intersection Points* process block.

Setup Incident Plane Wave for Requested Circular Polarisation: In order for the antenna to be processed as a LHC or RHC antenna, a second incident plane wave is necessary. According to [35] a circular polarised wave is created when $E_{ox} = E_{oy} = E_o$ and where $\varphi_y = \varphi_x \pm \pi/2$. The secondary incident plane wave is therefore described by:

$$E^{i\perp} = E_o\,[cos\left(\varphi + \frac{\pi}{2}\right)\boldsymbol{a_x} + sin\left(\varphi + \frac{\pi}{2}\right)\boldsymbol{a_y} + 0\boldsymbol{a_z}] \qquad 4.2$$

This secondary phase shifted incident wave has the same Poynting vector as the linear polarised wave, which are both in the negative z-direction.

Ray-Radome Outer Wall Intersection Points: The 3D positions where the incident ray penetrates the radomes outer surface are calculated here. Figure 4.7 shows the ray-radome puncture points for three different scan angles. These puncture points were calculated as follows:

- The 3D radome points were rotated about the radome parameter 'antenna pivot position'
- The x-y aperture positions are projected onto the rotated outer radome surface
- The intersection between the projections and the radome surface provides the z-value of the puncture points.
- The normal vector ($\hat{n}$) of the outer radome surface at each puncture point was also calculated and stored.

Figure 4.8 shows the puncture points and their normal (blue arrows) for the design case where the antenna aperture is rotated by 15°. The plane in which the antenna aperture lies is represented by the green surface.

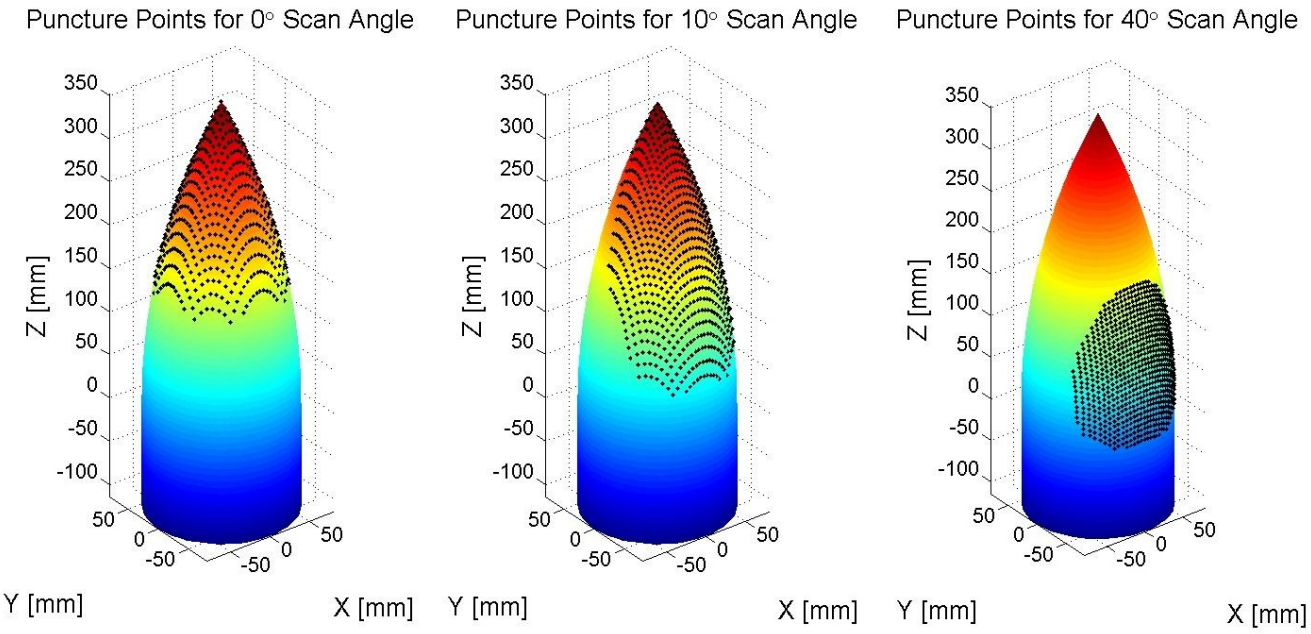

Figure 4.7: Radome-ray puncture points for three different scan angles.

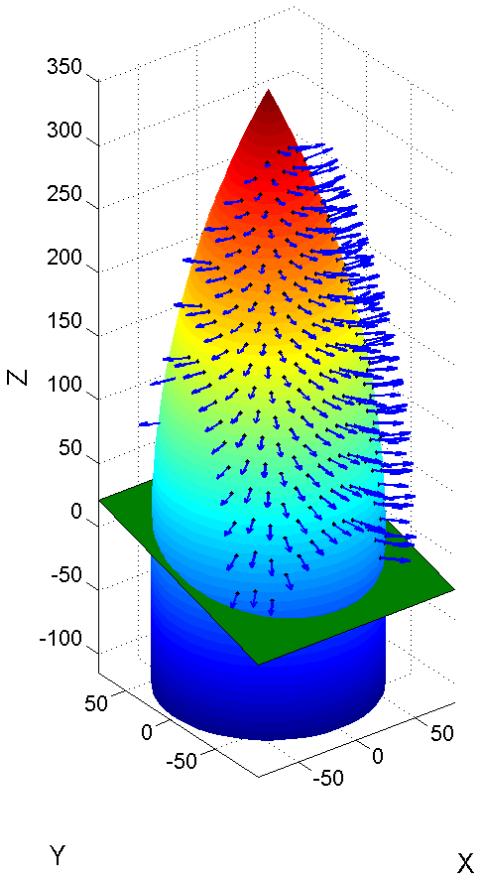

Figure 4.8: Normal vectors of the puncture points when the antenna aperture is scanned to 15°.

Radome Wall Thickness at each Intersection Point: When the radome wall taper (tp) is set to zero, no calculation is necessary and the wall thickness is uniform with a value of t. When tp is not zero, the resultant wall thickness is calculated by Eq. 4.3 below.

$$T_{wt} = \frac{-tp}{lr} z + t \qquad 4.3$$

T_{wt} is the resultant wall thickness and tp, lr and t have been defined in Table 4.1. This equation shows that the radome wall has a linear taper along the radome length, where the thickness at the radome base is t (z=0) whilst the thickness at the tip is $t + tp$.

The final step calculates the corresponding wall thickness at each puncture point. These wall thicknesses are used in the calculation of the reflection and transmission coefficients of the radome wall.

Incident Angle at each Intersection Point: The incident angle in the incident plane for each puncture point is calculated here. The *incident plane* is plane which contains the normal to the

surface and the incident ray. The incident angle (θ) is therefore the angle between the normal ($\hat{n}$) and the incident plane wave's Poynting vector ($\hat{S}$).

$$\|\hat{n} \times \hat{S}\| = \|\hat{n}\|\|\hat{S}\| sin(\theta) \quad 4.4$$

By rearranging Eq. 4.4, the incident angle is calculated by

$$\theta = sin^{-1}\left(\frac{\|\hat{n} \times \hat{S}\|}{\|\hat{n}\|\|\hat{S}\|}\right) \quad 4.5$$

EM Fields at each Intersection Point: The E-Fields are calculated at each intersection point by decomposing the incident fields into their TE and TM components. The vectors defining the TE and TM directions are defined by a_{te} and a_{tm} in the Eq. 4.6 and Eq. 4.7 respectively.

$$a_{te} = \hat{N} \times \hat{S} \quad 4.6$$

$$a_{tm} = a_{te} \times \hat{S} \quad 4.7$$

$\hat{N} = \hat{n}/\|\hat{n}\|$ is the normalised normal vector to the intersection point on the radome outer surface. The incident fields TE and TM components are calculated by Eq. 4.8 and Eq. 4.9 respectively.

$$E_{te} = (a_{te} \cdot E^i)a_{te} \quad 4.8$$

$$E_{tm} = (a_{tm} \cdot E^i)a_{tm} \quad 4.9$$

When the antenna is circularly polarised, the above calculations are undertaken for a second time with E^i replaced by $E^{i\perp}$ below.

$$E_{te\perp} = (a_{te} \cdot E^{i\perp})a_{te} \quad 4.10$$

$$E_{tm\perp} = (a_{tm} \cdot E^{i\perp})a_{tm} \quad 4.11$$

Reflection and Transmission at each Intersection Point: Either of the methods described in Chapter 2 or 3 could be used to determine the reflection and transmission coefficients at the intersection points. Equations 3.4 and 3.5 were used where the wall thickness l is calculated using Eq. 4.3. The transmission coefficients were calculated in both the TE (τ_{te}) and TM (τ_{tm}) directions.

Transmitted EM Fields through the Radome Wall: The total E-fields transmitted through the radome wall are calculated using Eq. 4.12 and Eq. 4.13 for the linear antenna polarisation and using Eq. 4.14 to Eq. 4.16 when the antenna is circularly polarised.

$$E_{Lin} = E_{te}\tau_{te} + E_{tm}\tau_{tm} \quad 4.12$$

$$E_{LinCoPol} = E_{Lin} \cdot E^{i} \quad 4.13$$

$$E_{Circ} = E_{te\perp}\tau_{te} + E_{tm\perp}\tau_{tm} \quad 4.14$$

$$E_{CircTotal} = E_{Lin} + E_{Circ}e^{j\frac{\pi}{2}\delta_p} \quad 4.15$$

$$E_{CircCoPol} = E_{CircTotal} \cdot E^{i} \quad 4.16$$

δ_p is the variable which is set according to the polarisation of the antenna [36]. When the polarisation is RHC, δ_p is -1, resulting in E_{Circ} lagging E_{Lin} by -90°. For LHC polarisation, E_{Circ} leads E_{Lin} by 90° and δ_p is set to +1. The co-polar fields calculated in Eq. 4.13 and Eq. 4.16 are the E-field components in the same direction as the incident E-field of the plane wave and are used in the following steps to calculate the BSE.

Project onto the Antenna Aperture Surface: The E-Fields calculated above are now projected onto the apertures surface. Monopulse tracking, used in this program, makes use of a sum and difference pattern to determine the position of the target. For this to happen, the antenna/antennas used must be able to operate or be processed in these different modes.

The antenna aperture is “simply” modelled as a four quadrant circular aperture. The co-polar fields of each individual quadrant are summed, weighted and then combined with the other quadrants. The weighting applied is dependent on the plane in which the antenna aperture is scanned and processed.

The resultant fields of each quadrant are calculated using Eq. 4.17 below.

$$E_{Q_i} = \sum_{n=1}^{N_A} E_{C_n} W_i \qquad i = 1, 2, 3, 4 \tag{4.17}$$

Where

i is the counter for each quadrant

n is the counter for each aperture puncture point in a quadrant

N_A is the total number of aperture puncture points of quadrant i

E_{Q_i} is the resultant E-field of quadrant i

W_i is the weighting of quadrant i

E_{C_n} is the co-polar field values incident on quadrant i

Depending on the antenna polarisation, E_{C_n} is either the $E_{LinCoPol}$ or $E_{CircCoPol}$ fields incident on quadrant i.

Calculate BSE: This final process block combines the fields calculated in the different quadrants to determine the BSE for a certain scan angle and incident plane wave polarisation.

The sum pattern is calculated for each quadrant by setting W_i to 1. The resulting antenna aperture sum pattern is calculated by Eq. 4.18 below.

$$E_{Sum} = E_{Q_1} + E_{Q_2} + E_{Q_3} + E_{Q_4} \qquad W_i = 1 \tag{4.18}$$

The difference patterns in two scan planes are calculated next. W_i is set according to the scan plane as defined in Figure 4.9. The difference patterns in the E- and H-plane scanning directions are given by Eq. 4.19 and Eq. 4.20 respectively.

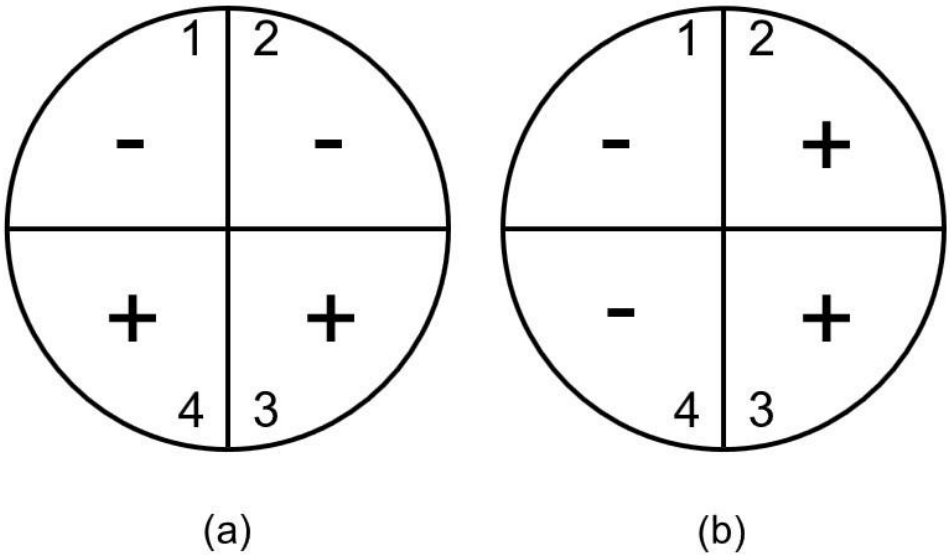

Figure 4.9: Aperture weighting for (a) E-plane (In-Plane) and (b) H-plane (Cross-Plane) scanning

$$E_{DiffE} = E_{Q_{1(W_i=-1)}} + E_{Q_{2(W_i=-1)}} + E_{Q_{3(W_i=1)}} + E_{Q_{4(W_i=1)}} \quad 4.19$$

$$E_{DiffH} = E_{Q_{1(W_i=-1)}} + E_{Q_{2(W_i=1)}} + E_{Q_{3(W_i=1)}} + E_{Q_{4(W_i=-1)}} \quad 4.20$$

The final step is to calculate the in-plane and cross-plane BSE. The two planes of BSE are defined by [37] as, "*In-plane* BSE is calculated by monopulse processing in the same plane as the aperture scan plane, i.e. azimuth scanning and azimuth monopulse BSE calculations. *Cross-plane* BSE is generated by performing monopulse processing in the plane orthogonal to the aperture scan plane, i.e. azimuth scanning and elevation monopulse BSE calculations." These definitions hold true for the BSE calculated next.

The full derivation of the BSE formula below is given in Appendix A.

$$BSE_E = K_E\, tan^{-1}(-Im(E_{DiffE}/E_{Sum})) \quad 4.21$$

$$BSE_H = K_H \tan^{-1}(-Im(E_{DiffH}/E_{Sum})) \quad 4.22$$

K_E and K_H are known as the sensitivity of the radome in the E- and H-Planes. The sensitivity is determined by the slope of the normalised difference pattern. [38]

4.3 Assumptions and Limitations

A number of assumptions were made in the ray tracing algorithm. Various limitations are placed on the parameter design ranges. These assumptions and limitations are listed and discussed next.

1) The algorithm considers only the ray-receive formulation. The reason for this is that it is simpler to describe propagation of an incident plane wave rather than propagation of the field near a radiating antenna [11]. Evanescent fields from radiating sources near the radome can couple directly to the curved slab and consideration of phenomena such as whispering gallery (WG) modes, creeping waves and slab guided modes would have to be taken into account if the transmit formulation was to be implemented [39].
2) Similar to [11] multiple scattering by the antenna, radome vertex and shell is ignored, as are surface waves along the radome wall. Internal reflections from the opposite wall and reflections from the bulkhead plate, if present, are not considered. Rays which do not intersect with the antenna aperture are ignored.
3) Unlike the ray tracing performed in [16], this code does not consider environmental conditions such as aerodynamic heating and ablation.
4) The code limits the radome profiles to bodies of revolution.
5) The dielectric used for the radome shell is considered to be lossless.
6) Uniform weighting is assumed across the antenna aperture.
7) The limitations applied to the radome parameters are shown in Table 4.2 below.

Table 4.2: Radome parameter limits

Input/Radome Parameter	Minimum	Maximum
Frequency	8 GHz	12 GHz
Dielectric relative permittivity	1	-
Radome wall thickness	$0.2\lambda_m$	$0.8\lambda_m$
Radome wall taper	$-0.15\lambda_m$	$0.15\lambda_m$
Radome fineness ratio	1.5	5
Antenna pivot position	0.9 lr	lr
Antenna aperture radius	-	0.95 ri
Incident wave polarisation angle	-90°	90°
Radome scan angle	0°	40°

The radome fineness ratio contains the limits controlling the radome length and base diameter. The inside radius of the radome (ri) is calculated by $ri = 0.5dr - t$.

4.4 Code Validation

The code written to calculate the BSE of an electrically large radome was validated against [38]. Here the tangent ogive shaped radome was modelled using flat plate theory and the antenna system worked in the ray-receive formulation. The incident fields on the radome were modelled as plane waves and were traced through the radome onto the antenna aperture using a ray tracing procedure. Singular internal reflections were considered, unlike the code described above. The antenna was scanned and the BSE was calculated for both in-plane and cross-plane scanning.

In 1995 the method described in [38] was expanded by [37]. The reference design of [38] and other research efforts of that time focussed on the scan angle dependence of BSE and results were limited to a number of polarisation cases. These efforts were able to identify scan regions possessing inherently greater BSE characteristics. The effort described in [37] extended these results by considering many more polarisation angles and the BSE sensitivity to these angles.

The radome design used to validate the MATLAB had radome parameters and properties listed below.

- Tangent ogive radome profile
- X-Band frequency
- Radome length: 30λ
- Radome base diameter: 10λ
- Constant wall thickness: 0.3166λ
- Relative permittivity: 3.2
- Tan delta (tanδ): 0.008
- Gimbal position (from the radome base): 2λ
- Aperture diameter: ±8λ
- 208 Element aperture with uniform weighting and RHC polarised elements
- E-field polarisation angle varies between ±90°
- The aperture scan angle varies between 0° to 40°.
- Sensitivity of the Radome (K_E = K_H = $0.6357\ dr/\lambda$)

The predicted BSE for this design are presented in the figures which follow. Figure 4.10 shows the overlay for the in-plane scanning design situation whilst Figure 4.11 shows the cross-plane design. The reference surfaces from [37] are represented by the black mesh in these figures. A number of polarisation angle versus scan angle traces are selected for both scanning directions and are shown in Figure 4.12 and Figure 4.13.

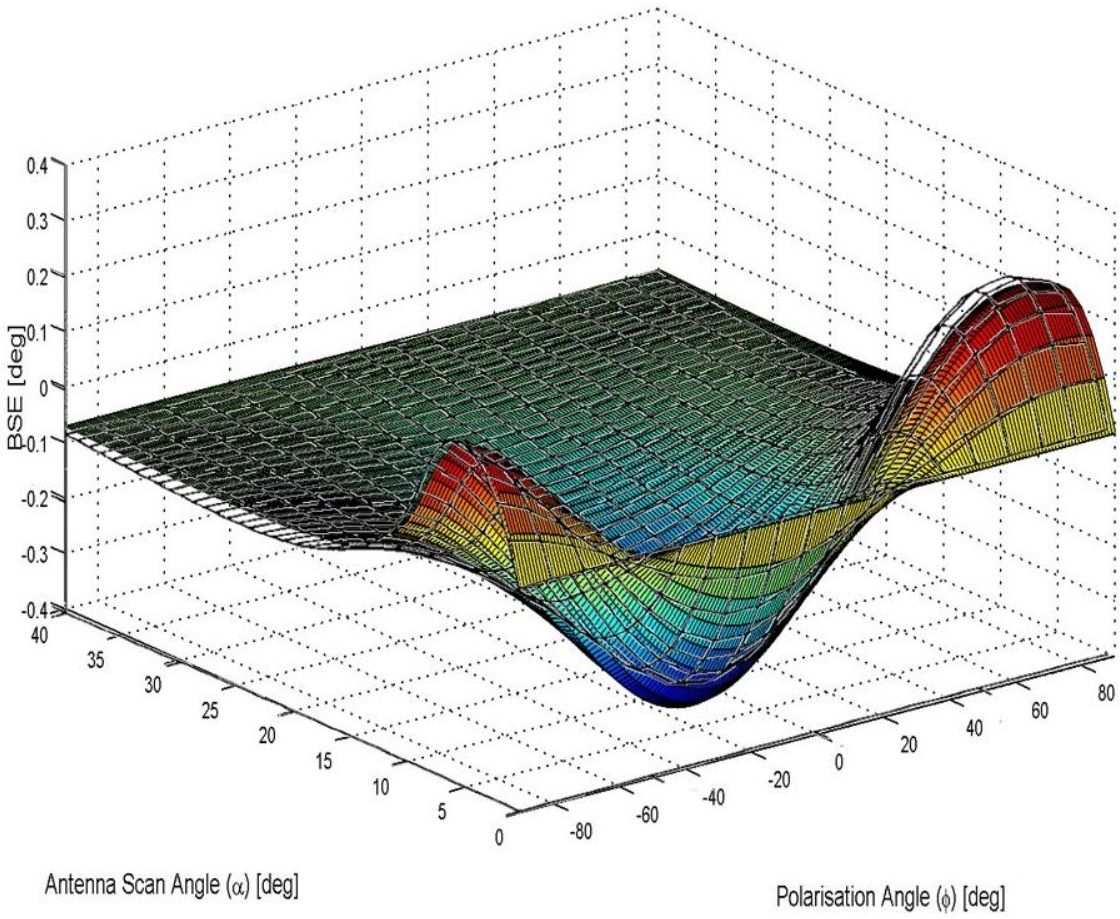

Figure 4.10:In-Plane scanning BSE with literature results overlaid.

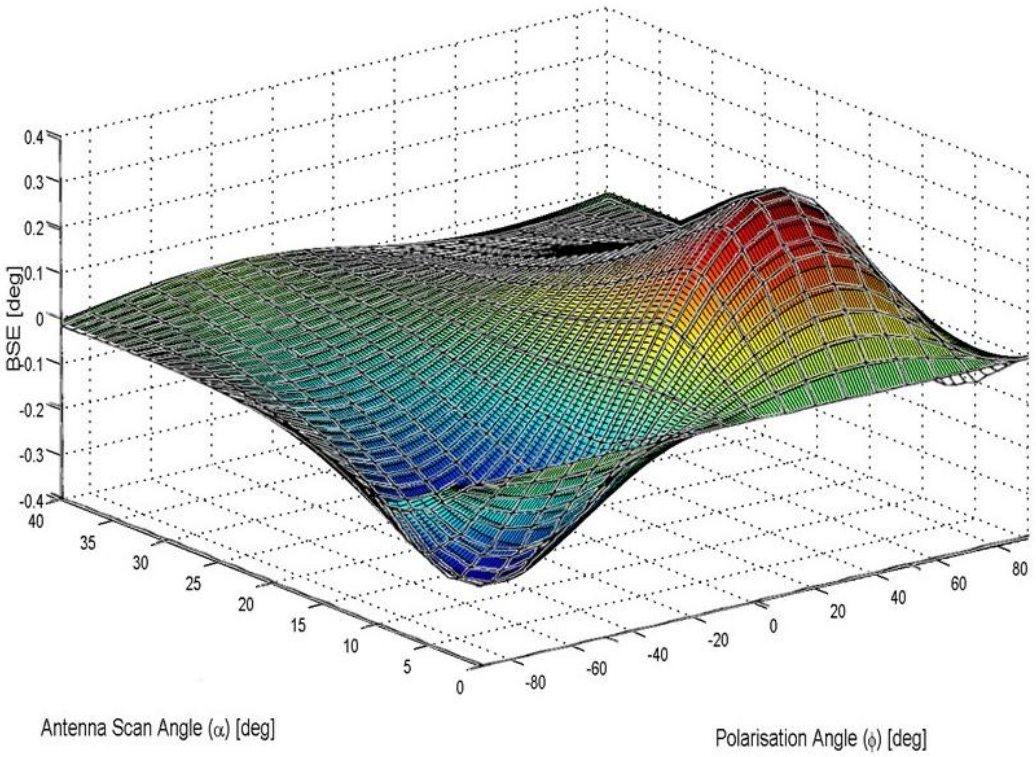

Figure 4.11: Cross-Plane scanning BSE with literature results overlaid.

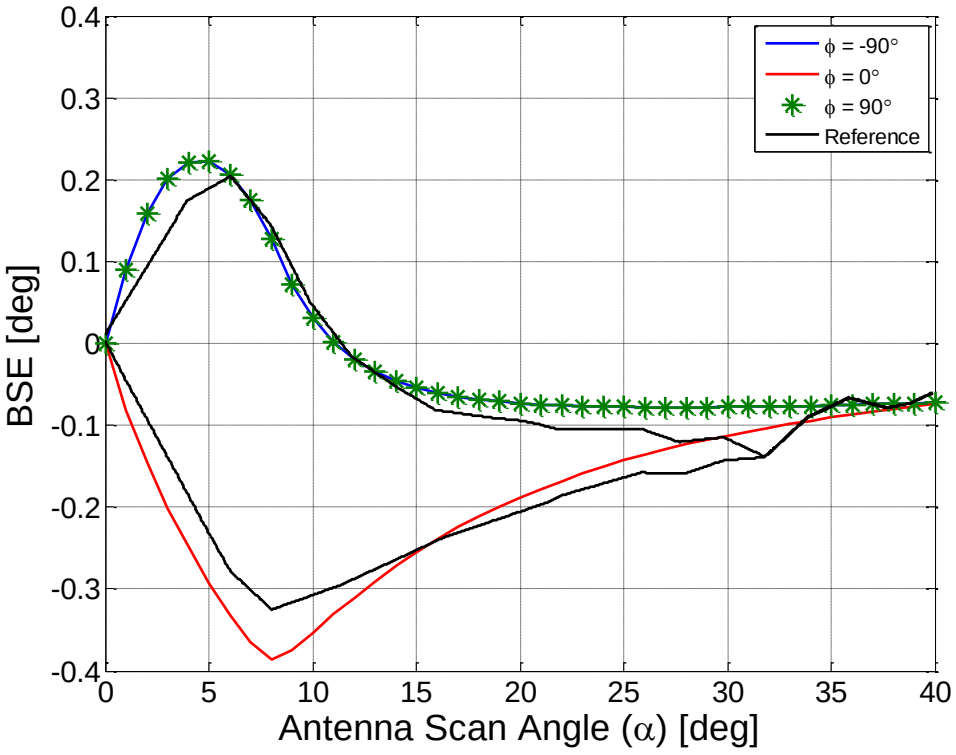

Figure 4.12: In-Plane scanning BSE vs Reference for various polarisations.

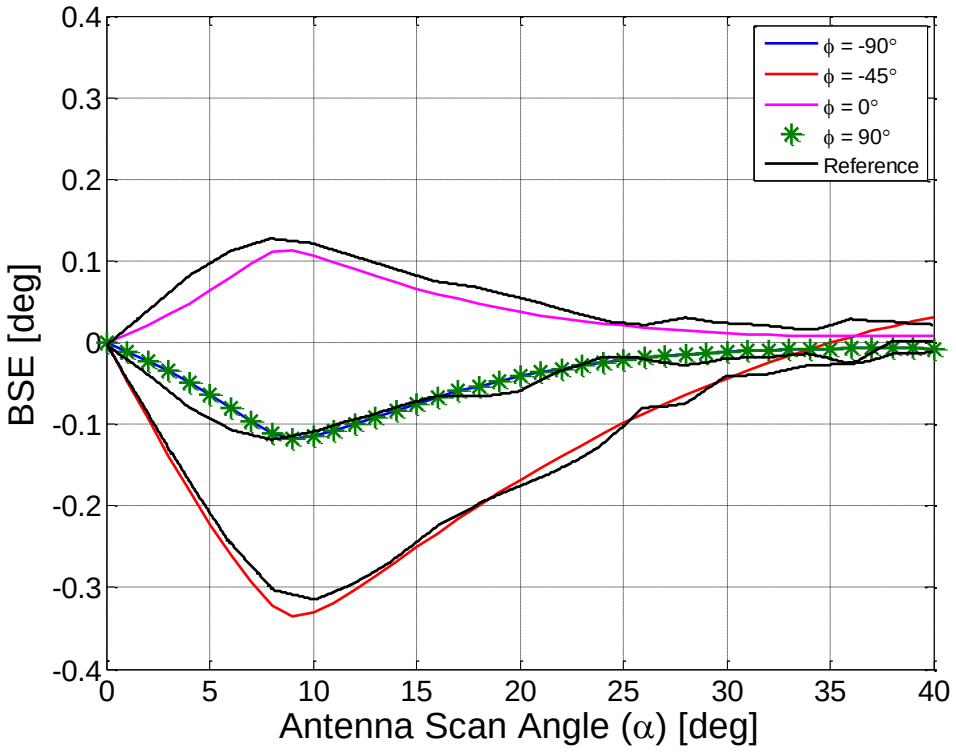

Figure 4.13: Cross-Plane scanning BSE vs Reference for various polarisations.

The reference data was obtained from [38] using the "chart tracing tool" of the antenna design software, Antenna Magus[2]. This was done so that accurate data could be captured and used for validation. As may be seen, the agreement between the literature and MATLAB code for both in- and cross-plane scanning is acceptable. The maximum difference in error for in-plane scanning was 0.06° whilst a maximum difference in error of 0.03° for the cross-plane scanning was observed.

A second set of simulations was undertaken where the polarisation of the antenna was changed from RHC to linearly polarised. The results of these simulations are shown in Figure 4.14 and Figure 4.15.

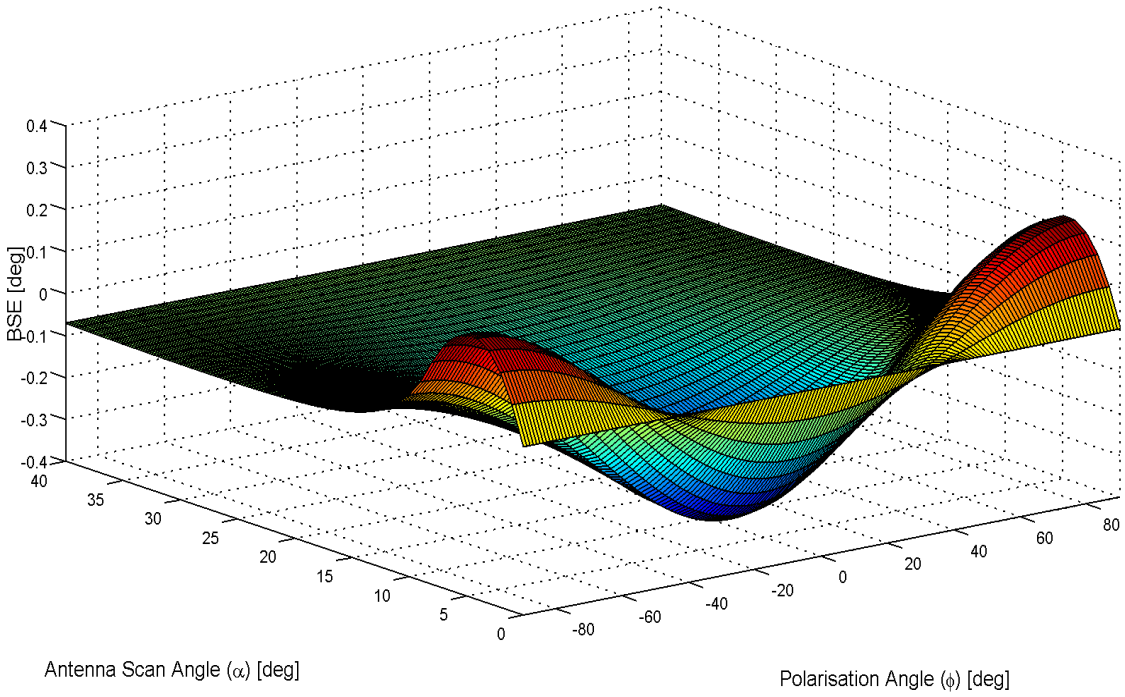

Figure 4.14: In-Plane scanning BSE results for a linearly polarised antenna.

[2] For more information,
please visit http://www.antennamagus.com/

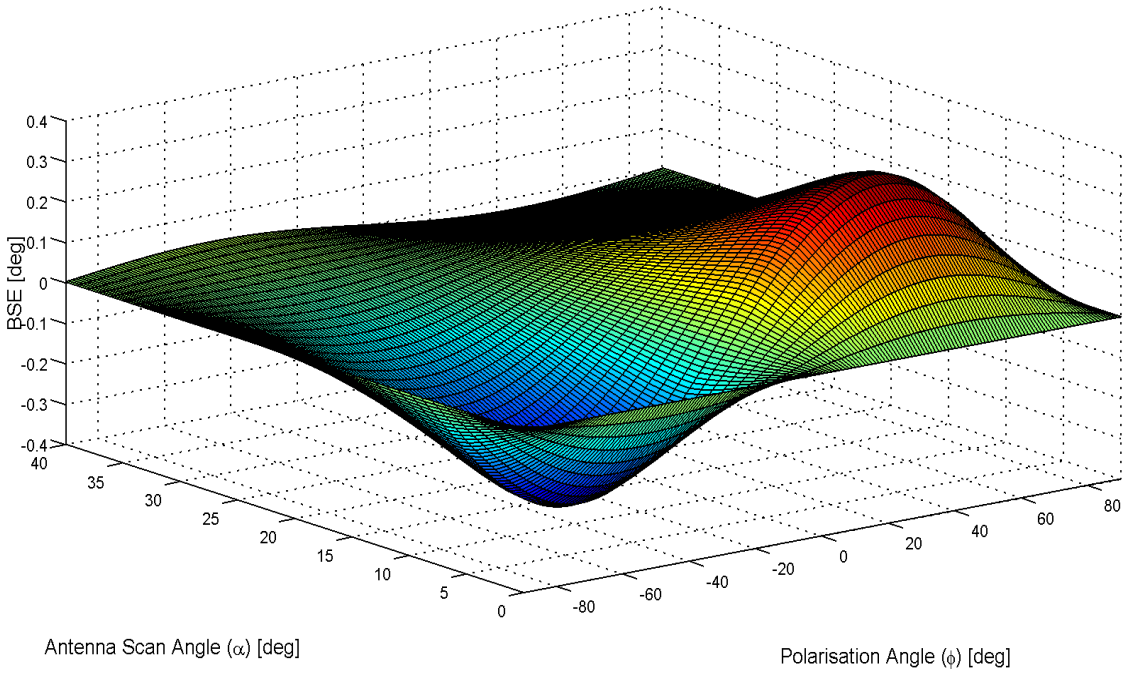

Figure 4.15: Cross-Plane scanning BSE results for a linearly polarised antenna.

The BSE results clearly indicate the following [37]:

- For circularly polarised antenna, the BSE is heavily dependent on both the scan angle and the reference E-field polarisation.
- Given a linearly polarised antenna, the BSE is primarily dependent on aperture scan angle and less sensitive to changes in reference E-field polarisation.

It was noted that the cross-plane BSE exists for a purely TE/TM incident plane wave even though the radome-induced distortion has reflection symmetry about the y = 0 plane in Figure 4.6. This is due to the RHC component of the field being sensed by the circularly polarised (CP) antenna. The CP antenna does not have mirror symmetry about y = 0 plane, therefore this cross-plane BSE can exist even when symmetrically distorted fields are present. A TE/TM linearly polarised antenna will not have cross-plane BSE when a same sensed incident field is present. This statement has been validated as seen in Figure 4.15. [38]

An earlier suggestion for the elimination of BSE was to have a look-up calibration table which could effectively calibrate the BSE out. BSE could be calibrated out as a function of the antennas scan angle for all possible receive polarisations. This was proven to not be possible by [37]. The BSE, as can be seen by the results above, is dependent on both the aperture scan angle and the incident polarisation once again suggesting that the look-up table method would be insufficient.

The results also show that the BSE is greatest for small aperture scan angles, typically from 0° to 15°. This region has been identified as the area of worst case BSE [37]. This can be put down to tip scatter and surface waves being introduced, and because of the large distortion to the fields in this region with a small radius of curvature.

4.5 Graphical User Interface (GUI)

In order to make the code more practical and 'user friendly', a user interface was designed and is presented in Figure 4.16 below. The user interface is designed to (1) capture all the radome design information, (2) execute the ray tracing procedure and (3) present the results of the design. This interface can also be used to facilitate the optimising of individual/multiple parameters and determining the change in BSE response.

The flow diagram for the user interface is the same as that in Figure 4.1. A number of hidden features are present in this user interface and they will be summarised below.

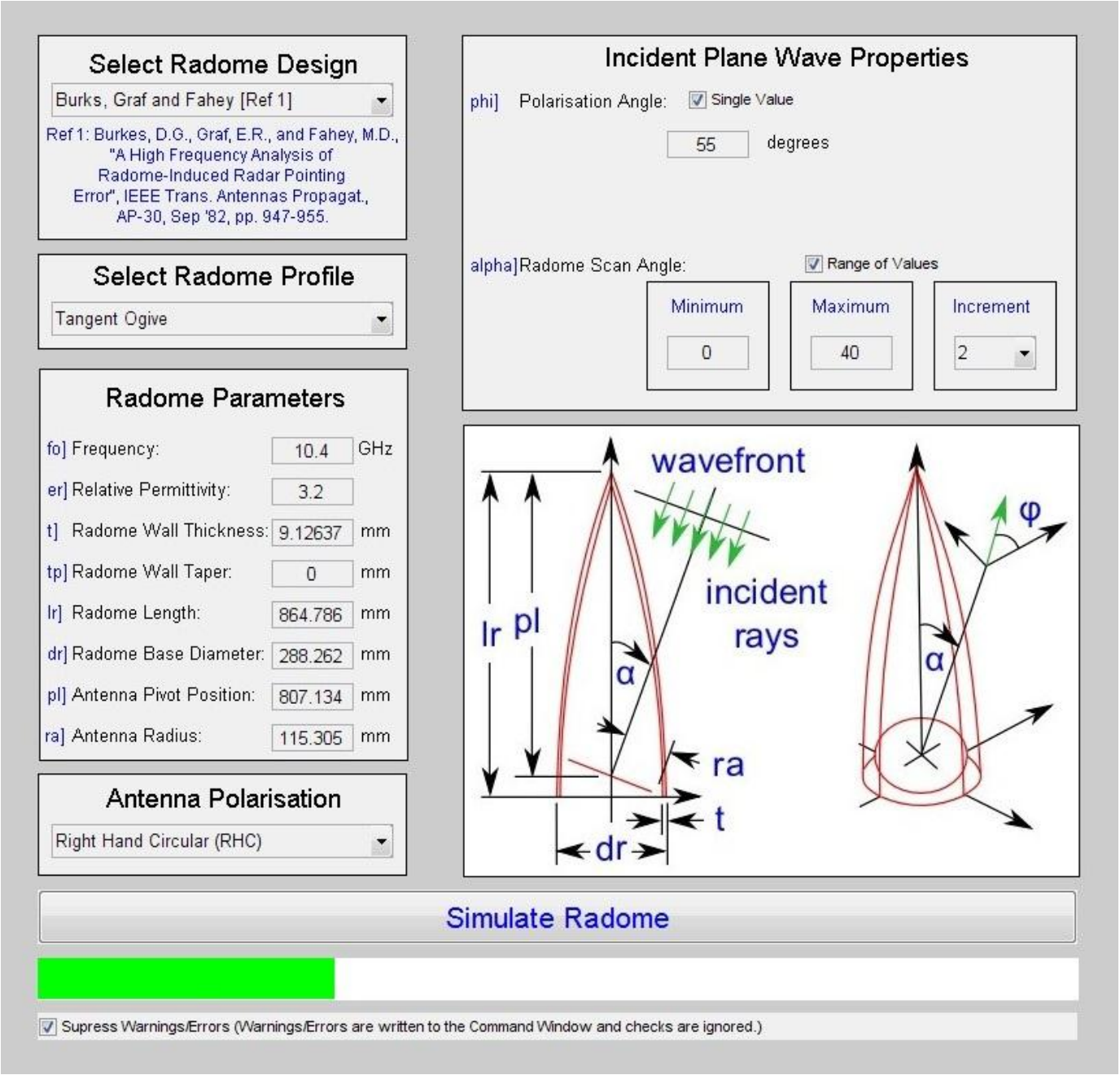

Figure 4.16: User interface layout.

The first is the dropdown menu under the 'Select Radome Design' pallet. Three options are present of which the first two options are design cases, which when selected, will enter a set of radome parameters which are ready to simulate. The third option is for a custom design. When this field is selected, all the parameter fields are left blank for custom values to be entered. Figure 4.16 has the design case, presented in the validation section above, selected.

The radome profile is selected by the dropdown menu under the 'Select Radome Profile' pallet. The options are (1) tangent ogive, (2) half power series and (3) Von Kaman. Both standard design cases are for tangent ogive radome profiles.

The pallet, 'Radome Parameters' is used to capture all the radome parameter values. These values are checked according to the limitations stated in Table 4.2 section and will inform the user if any of these limits have been breached. An extra feature at the bottom of the user interface is used to ignore all the warnings. When selected the various warnings are written to the command window and are ignored. Erroneous results may be achieved due to design parameters which do not fall within the limitations. The author takes not responsibility for this.

The antenna polarisation is selected from the drop down menu in the 'Antenna Polarisation' pallet. RHC, LHC or linear polarisation are the 3 options supported.

The final pallet to be filled in is used to capture the incident wave properties. As described previously, the polarisation and scan angles may be a single value or a series of values between a minimum and a maximum value with a set angle increment. An extra check box is present (not in Figure 4.16) which will simulate only the TE and TM polarisation cases.

Once all the pallets have been successfully filled in and the data has been captured, the design may be executed by clicking on the 'Simulate Radome' button. A progress indication bar at the bottom of the user interface is used to monitor the progress of the simulation.

The results of the design are presented to the user in a graphical form similar to the results shown in Chapter 4.4 above.

5 Results

This Chapter will discuss the results obtained through the use of the user interface and ray tracing code.

5.1 Ray Tracing Results

Chapter 4 described the design of the ray tracing code and user interface in extensive detail. The results obtained for the literature validation design case were accurate and are presented in Chapter 4.4. These results will not be repeated here for brevity.

5.2 Similar Code Comparison

To ensure the validity of the method discussed in Chapter 4, a second reference was obtained from Mr J. Joubert [40]. This reference uses a very similar ray tracing method to obtain BSE results for a tangent ogive shaped radome. The principle, TE and TM, incident wave polarisations are compared in Figure 5.1 below.

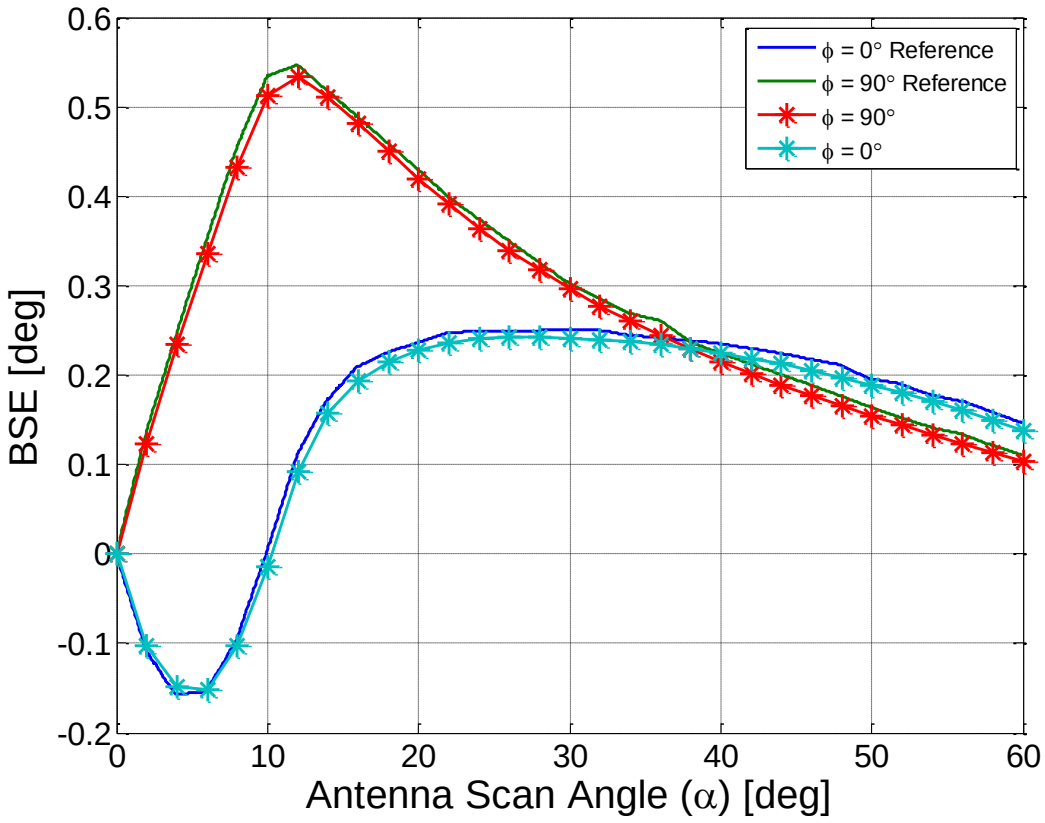

Figure 5.1: In-plane BSE comparison between ray tracing code and [40]

The incident wave polarisation angle definitions were different between the two sets of results. This was the only adjustment that was made in order to plot the traces correctly for direct comparison. A good agreement was achieved for both polarisations. This second validation case proves that the code produces correct results and that the validation of [38] was not a once off phenomenon.

Through the use of the GUI, a total time of 2 minutes was needed to set all the design parameters, simulate the design problem and produce the results present in Figure 5.1. This design situation proved the ease and speed at which a result for an electrically large radome can be obtained through the use of the GUI and ray tracing code.

5.3 Optimised Design

One of the features of the GUI is to provide the user with the ability to change radome parameters, simulate the design problem, and within a very short time, see the effect which the parameter changes had on the radomes BSE performance. This allows the design of the radome

and thereafter the optimisation of individual parameters. This process will be described next through an example.

The radome [38] used for the code validation in Chapter 4 was used as the initial design. By changing the wall thickness variable, a change in BSE performance was achieved. By decreasing the wall thickness, the BSE was worse than the original design. By increasing the wall thickness, the BSE was reduced.

The wall thickness parameter was further optimised through the use of the user interface. Within 10 minutes, a wall thickness was designed which significantly reduced the BSE in the "region of worst case BSE". Not only was the BSE reduced, the important BSES is "flatter" and less variant than the original design. The BSE results for the TE and TM incident polarisations are shown in Figure 5.2 and BSES results in Figure 5.3. A comparison of the original wall thickness and the optimised thickness are shown in Table 5.1 below.

Table 5.1: Comparison of wall thickness values for optimisation

	Burks Radome [38]	**Optimised Radome**
Wall Thickness (mm)	9.126	9.57
Electrical Wall Thickness (λ_m)	0.566	0.59

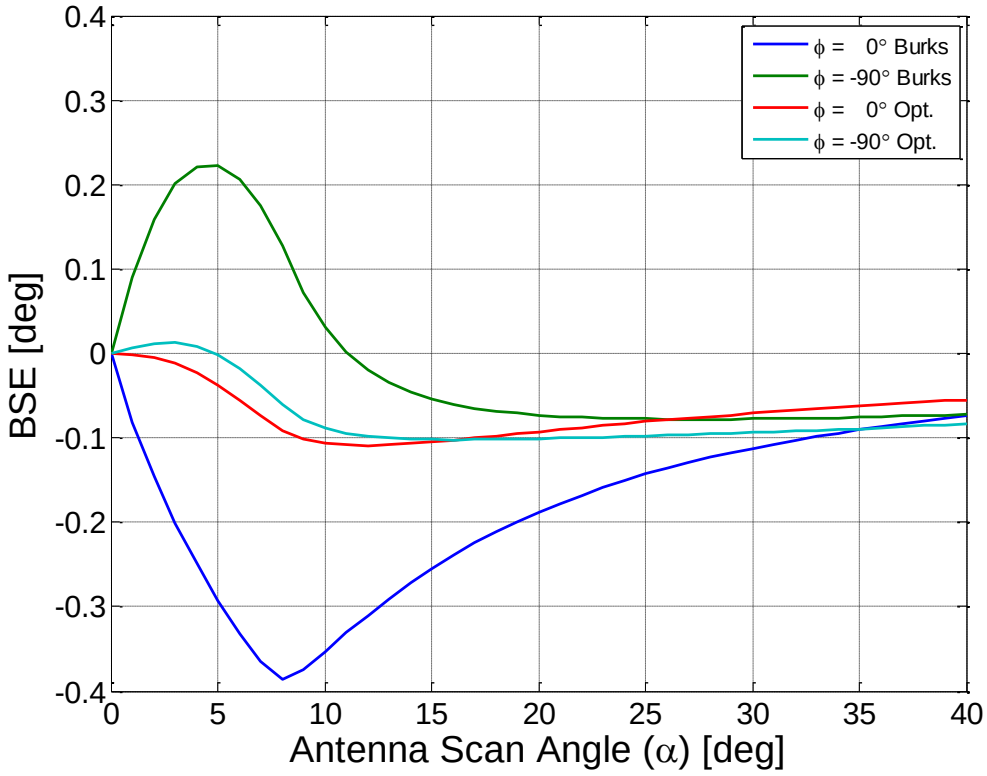

Figure 5.2: BSE results for original versus optimised design

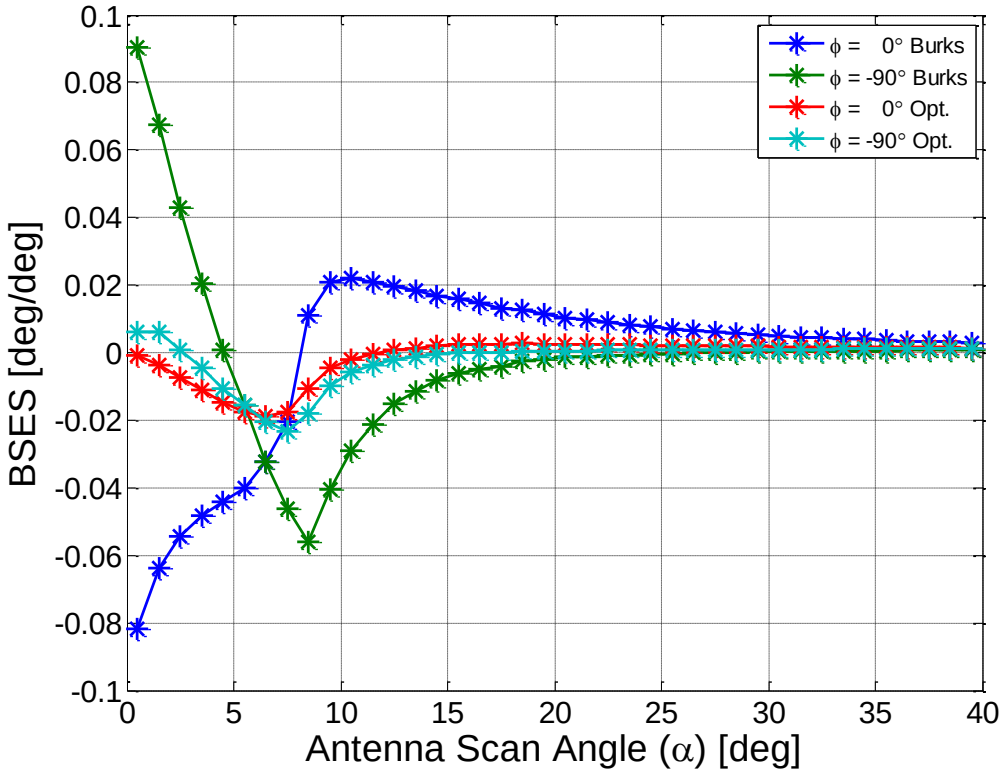

Figure 5.3: BSES results for original versus optimised design

Both results show a much improved response than the original radome design. The BSES in Figure 5.3 is much more favourable than the original result. The worst BSES for the optimised design is -0.02 deg/deg whilst the original design is 0.09 deg/deg. This is 4 ½ times better than that of the original design.

The user interface, together with the ray tracing code, provides very quick results to electrically large radome designs. The optimisation example shows that a radome designer can obtain valuable insight into a problem in a short period of time with very little effort.

6 General Conclusion

The analysis and design of electrically large radomes for seeker applications has been a difficult and time consuming task for many years. The objective of this thesis was to develop a quick ray tracing approach, together with a graphical user interface, to aid in the design and analysis of electrically large radomes.

These objectives were achieved by first gaining an understanding of the general problems surrounding radome design. Mechanical, electrical and environmental design considerations were researched, and thereafter, EM techniques used to solve seeker radome problems.

Further understanding of the radome problems was obtained through the development of the visual 2D ray tracing code, where various methods used in the final ray tracing approach were developed and validated.

The ray tracing approach developed produced BSE results which were very accurate when compared to literature. A second radome design was obtained for comparison with the code developed. This too produced very accurate results verifying the validity of the code.

The final objective of this thesis was to develop a GUI which is used to interface with the ray tracing code. The GUI was successfully implemented and through the use of a final design case, demonstrated that it can be used to control optimisation and parameter changes very easily, in minimal time.

In conclusion, the GUI interfaced ray tracing tool developed here is useful in analysing the impact of parameter changes to a defined radome. The use of such a code will reduce the amount of testing associated with radome design and can therefore be seen as cost effective.

Recommendations for further research would be the addition of the following points to the code and user interface:

- Specify the metallic tip on the end of the radome. The bluffness ratio is used to specify this and the modelling requires that any ray intersecting the tip is to be ignored.
- Ability for the code to handle reflections from the internal walls. These reflections were shown by [38] to be a major cause to radome BSE.
- Add the ability to apply different weightings to the antenna aperture. This can be done by a few standard distributions, such as raised cosine, or a tabular method for input.
- Ability to specify a multi-layered (sandwich) radome wall. Each layer should have a permittivity, thickness and taper.

All these recommendations will model the actual radome problem with more accuracy and provide results which closer reflect reality.

Appendix A: Tracking Error

The formula used to calculate the tracking errors of a radome are defined by Eq. 4.21 and Eq. 4.22. The derivation of these equations will be discussed through the use of Figure A1.

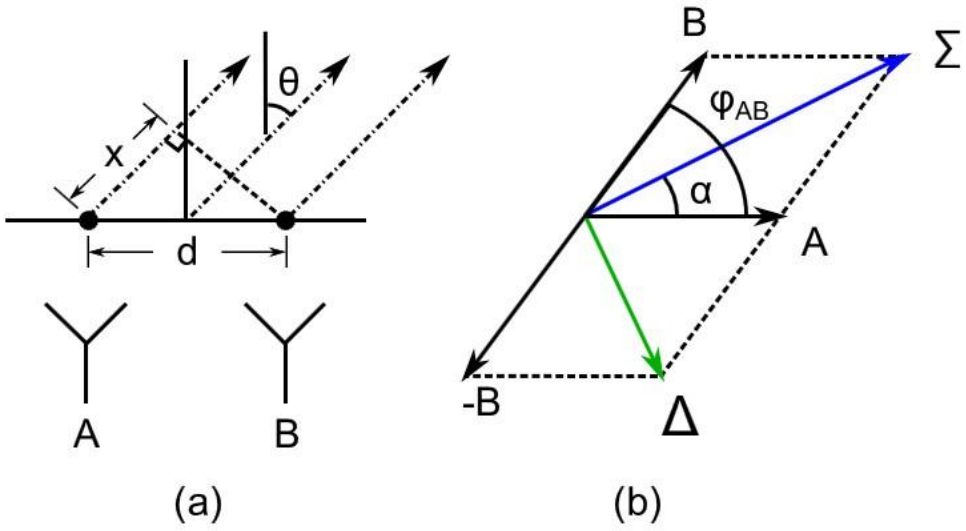

Figure A1: (a) Physical antenna setup; (b) vectors used for the sum and difference calculations

A linear arrangement of two antennas, A and B, that are separated by a distance, d, and have a signal incident from an angle, θ, are shown in Figure A1 (a). The phase difference between A and B is defined by Eq. A1. This well-known formula will not be derived.

$$\Delta\varphi_{AB} = \frac{2\pi d sin\theta}{\lambda} \qquad \text{A1}$$

This equation shows that when the incident angle is zero, the phase difference between the antennas is also zero.

Figure A1 (b) will be used to define the tracking error. Antenna A will be used as the reference antenna. The phase difference between A and B, is defined by the angle φ_{AB}.

Vectors A and B are defined by the following:

$$A = 1\angle 0 = e^{j0} \quad \text{A2}$$

$$B = 1\angle \varphi_{AB} = e^{j\varphi_{AB}} \quad \text{A3}$$

The tracking error is calculated using the sum and difference patterns. From Figure A1(b) the sum is defined as A+B and the difference by A-B. Euler's formula, Eq. A4, will be used to derive the tracking error.

$$e^{j\theta} = cos\theta + jsin\theta \quad \text{A4}$$

The sum ($\sum$) and difference (Δ) can now be defined by:

$$\sum = A + B = 1 + e^{j\varphi_{AB}} \quad \text{A5}$$

$$\Delta = A - B = 1 - e^{j\varphi_{AB}} \quad \text{A6}$$

Using Eq. A4, the sum and difference can be written as:

$$\sum = 1 + cos\varphi_{AB} + jsin\varphi_{AB} \quad \text{A7}$$

$$\Delta = 1 - cos\varphi_{AB} - jsin\varphi_{AB} \quad \text{A8}$$

The phase angle, φ_{AB}, is now substituted by 2α so that double and half angle identities can be used. The identities used are listed below.

$$cos2\alpha = 2cos^2\alpha - 1 \quad \text{A9}$$

$$cos2\alpha = 1 - 2sin^2\alpha \quad \text{A10}$$

$$sin2\alpha = 2(cos\alpha)(sin\alpha) \quad \text{A11}$$

Eq. A7 and Eq. A8 can now be written as

$$\sum = 1 + cos2\alpha + jsin2\alpha \quad \text{A12}$$

$$\Delta = 1 - cos2\alpha - jsin2\alpha \quad \text{A13}$$

By substituting Eq. A9 and Eq.A11 into Eq. A12, the sum can now be written as

$$\sum = 2cos\alpha(cos\alpha + jsin\alpha) \quad \text{A14}$$

By substituting Eq. A10 and Eq. A11 into Eq. A13, the difference can now be written as

$$\Delta = -2jsin\alpha(cos\alpha + jsin\alpha) \quad \text{A15}$$

Using Eq. A4 once again, Eq. A14 and Eq. A19 can be simplified to

$$\sum = 2cos\alpha \cdot e^{j\alpha} \quad \text{A16}$$

$$\Delta = -2jsin\alpha \cdot e^{j\alpha} \quad \text{A17}$$

The tracking error is now determined by the following ratio:

$$\frac{\Delta}{\sum} = -jtan\alpha \quad \text{A18}$$

Eq. A18 can now be changed so that α is the subject of the formula, which is the tracking error.

$$\alpha = tan^{-1}(-Im(\frac{\Delta}{\sum})) \quad \text{A19}$$

References

[1] S. S. Chin, “Missile Configuration Design,” McGraw-Hill Book Company, Inc., 1961.

[2] G. A. Crowell, “The Descriptive Geometry of nose cones,” 1996. [Online]. Available: http://projetosulfos.if.sc.usp.br/artigos/NoseCone_EQN2.PDF. [Accessed 1 September 2012].

[3] F. D. Groutage, “Radome development for broadband RF missile sensor,” Technical Report No. TR2023, Naval Electronics Laboratory Centre, San Diego, California, January 1977.

[4] J. L. Volakis, “Chapter 53: Radomes,” in *Antenna Engineering Handbook, Fourth Edition*, McGraw-Hill, 2007.

[5] S. Silver (ed.), “Radome Design Problems and Procedures,” in *Microwave Antenna Theory and Design*, New York, McGraw-Hill, 1949, pp. 522-542.

[6] D. M. Pozar, “Microwave Network Analysis,” in *Microwave Engineering, 2nd Edition*, John Wiley & Sons, 1998, pp. 206-213.

[7] T. A. Milligan, “Chapter 2: Radiation Structures and Numerical Methods,” in *Modern Antenna Design*, New York, McGraw-Hill, 1985, p. 93.

[8] D. A. Conti, “Special problems associated with aircraft radomes,” *Communications, Radar and Signal Processing, IEE Proceedings F,* vol. 128, no. 7, pp. 412-418, December 1981.

[9] B. Rulf, “Problems of Radome Design for Modern Airborne Radar,” *Part 1, Microwave Journal,* vol. 28, no. 1, pp. 145-152, January 1985.

[10] B. Rulf, “Problems of Radome Design for Modern Airborne Radar,” *Part 2, Microwave Journal,* vol. 28, no. 5, pp. 265-271, May 1985.

[11] G. Tricoles, “Radiation Patterns and Boresight Error of a Microwave Antenna Enclosed in an Axially Symmetric Dielectric Shell,” *Journal of the Optical Society of America,* vol. 54, no. 9, pp.

1094-1101, September 1964.

[12] D. J. Kozakoff, “Chapter 8: Radome-Enclosed Guidance Antennas,” in *Analysis of radome-enclosed antennas*, Artech House, 1997, pp. 157-184.

[13] M. L. Skolnik, “Chapter 4: Tracking Radar,” in *Introduction to Radar Systems, 3rd Edition*, New York, McGraw-Hill, 2010, pp. 210-224.

[14] T. E. Tice, “Techniques for airborne radome design,Volume One,” USAF Report AFATL-TR-66-391 Volume 1, McGraw-Hill, 1966.

[15] T. E. Tice, “Techniques for airborne radome design, Volume Two,” USAF Report AFATL-TR-66-391 Volume 2, McGraw-Hill, 1966.

[16] T. S. Pendergrass, “Radome Analysis,” Contract DASG60-81-C-0109, U S Ballistic Missile Defence Command AD-A136805, Huntsville, Alabama, October 1983.

[17] D. J. Kozakoff, “Chapter 6:Radome Analysis Techniques,” in *Analysis of radome-enclosed antennas*, Artech House, 1997, pp. 103-123.

[18] Mahan, A.I., C.V. Bitterli, and C.G. Wein, “Far Field Diffraction and Boresight Error Properties of a Two Dimensional Wedge,” *Journal of the Optical Society of America,* vol. 49, no. 6, pp. 535-566, June 1959.

[19] T. A. Milligan, “Chapter 2: Radiation Structures and Numerical Methods,” in *Modern Antenna Design*, New York, McGraw-Hill, 1985, pp. 84-85.

[20] Hayward, R. A., E. L. Rope, and G. Tricoles, “Accuracy of Two Methods for Numerical Analysis of Radome Electromagnetic Effects,” in *IEEE International Symposium Digest on Antennas and Propagation*, Seattle, June 1979.

[21] J. A. Shifflett, “CADDRAD: A Physical Optics Radar/Radome Analysis Code for Arbitrary 3D Geometries,” *IEEE Antennas and Propagation Magazine,* vol. 39, no. 6, pp. 73-79, 1977.

[22] E. B. Joy, “Comparison of Radome Electrical Analysis Techniques,” in *Proceedings of the 15th Symposium on Electromagnetic Windows*, Georgia Institute of Technology, Atlanta, GA, 1980.

[23] Hayward, R. A., E. L. Rope, and G. Tricoles, “Analysis of Radomes by the Method of Moments Method,” in *Proceedings of the 17th Symposium on Electromagnetic Windows*, Georgia Institute of Technology, Atlanta, GA, 1984.

[24] Lo, Y.T., and S.W. Lee, “Radiation from Apertures,” in *Antenna Handbook Volume 2*, New York, Van Nostrand Reinhold, 1993, pp. 5.1-5.34.

[25] Wu, D.C.F., and R.C. Rudduck, “Plane Wave Spectrum Surface Integration Technique for Radome Analysis,” *IEEE Transactions on Antennas and Propagation,* Vols. AP-22, no. 3, pp. 497-500, May 1974.

[26] Chang, J.H., and K.K. Chan, “Analysis of a two-dimensional radome of arbitrarily curves surface,” *IEEE Transactions on Antennas and Propagation,* vol. 38, no. 10, pp. 1559-1568, October 1990.

[27] Maloney, J. G., and G. S. Smith, “Modeling of Antennas,” in *Advances in Computational Electrodynamics*, A. Taflove, (ed.), Norwood, MA:, Artech House, 1998, pp. 453-456.

[28] Sukharevsky, O. I., S. V. Kukobko, and A. Z. Sazonov, “Volume Integral Equation Analysis of a Two Dimensional Radome with a Sharp Nose,” *IEEE Transactions and Propagation,* vol. 53, no. 4, pp. 1500-1506, April 2005.

[29] Kukobko, S.V., A.Z. Sazonov, and O.I. Sukharevsky, “Mathematical simulation of reflector-type antenna ith sharp nose radome scattering (two-dimensional problem),” in *Antenna Theory and Techniques*, May 2005.

[30] Moneum, M. A., et al, “Hybrid PO-MOM Analysis of Large Axis-Symmetric Radomes,” *IEEE Transactions on Antennas and Propagation,* vol. 49, no. 12, p. 1657–1660, December 2001.

[31] S. J. Orfanidis, Electromagnetic Waves and Antennas, Rutgers University, 2008.

[32] Garg, R., P. Bhartia, I. Bahl and A. Ittipiboon, “Chapter 1.5: Surface Waves and Photonic Bandgap Structures,” in *Microstrip Antenna Design Handbook*, Artech House, 2001, pp. 43-53.

[33] "Private communication".

[34] Petersson, L.E.R., and G.S. Smith, “On the use of a Gaussian Beam to isolate the edge scattering from a plate of finite size,” *IEEE Transactions on Antenna Propagation,* vol. 52, no. 2, pp. 505-512, February 2004.

[35] Guru, B.S., and H.R. Hiziroglu, Electromagnetic Field Theory Fundamentals, Boston: PWS Publishing Company, 1998.

[36] Stutzman, W.L., and G. A. Thiele, “Chapter1: Antenna Fundamentals and Definitions,” in *Antenna Theory and Design, 2nd edition*, New York, John Wiley, 1998, p. 51.

[37] Wilson, K.S.; V.P. Pyati, and M.A. Temple, “Dependance of monopulse radar boresight error on incident E-field polarization,” in *IEEE International Radar Conference*, May 1995.

[38] Burks, D.G., E.R. Graf, and M.D. Fahey, “A High Frequency Analysis of Radome-Induced Radar Pointing Error,” *IEEE Transactions o Antennas and Propagation,* vol. 30, no. 5, pp. 947-955, September 1982.

[39] N. Subramaniam, “Wave Propagation Through Curved Shells and the Validity of the Plane-Slab Approximation,” *IEEE Transactions and Propagation,* vol. 39, no. 9, pp. 1265-1271, Spetember 1991.

[40] "Private communication".